ARTICLES
https://doi.org/10.1038/s41593-021-00820-w

nature neuroscience

Check for updates

An emergent neural coactivity code for dynamic memory

Mohamady El-Gaby[1,2]✉, Hayley M. Reeve[1], Vítor Lopes-dos-Santos[1], Natalia Campo-Urriza[1], Pavel V. Perestenko[1], Alexander Morley[1], Lauren A. M. Strickland[1], István P. Lukács[3], Ole Paulsen[2] and David Dupret[1]✉

Neural correlates of external variables provide potential internal codes that guide an animal's behavior. Notably, first-order features of neural activity, such as single-neuron firing rates, have been implicated in encoding information. However, the extent to which higher-order features, such as multineuron coactivity, play primary roles in encoding information or secondary roles in supporting single-neuron codes remains unclear. Here, we show that millisecond-timescale coactivity among hippocampal CA1 neurons discriminates distinct, short-lived behavioral contingencies. This contingency discrimination was unrelated to the tuning of individual neurons, but was instead an emergent property of their coactivity. Contingency-discriminating patterns were reactivated offline after learning, and their reinstatement predicted trial-by-trial memory performance. Moreover, optogenetic suppression of inputs from the upstream CA3 region during learning impaired coactivity-based contingency information in the CA1 and subsequent dynamic memory retrieval. These findings identify millisecond-timescale coactivity as a primary feature of neural firing that encodes behaviorally relevant variables and supports memory retrieval.

What features of neural activity does the brain use to encode information about the external world? Ample evidence suggests that firing rates[1,2] and temporal tuning properties[3,4] of individual neurons show robust correlations with external variables. These first-order features of neural activity could serve as neural codes that are read by downstream structures to subsequently guide behavior[5]. Moreover, advances in in vivo multiunit recordings have allowed further appreciation for the role of neuronal population dynamics in supporting internal representations[6–8]. The timescale at which population activity is organized may be critical. In particular, coincidental spiking at the timescale of a neuron's membrane time constant (~10–30 ms for cortical neurons[9]) effectively drives downstream receiver neurons[5,10], can be parsed within network oscillations that pace firing of neuronal populations[5] and can be rapidly stabilized through spike-timing-dependent plasticity (STDP)[11,12]. Indeed, millisecond-timescale coactivity is a hallmark of some neural codes[13–15]. Such short-timescale coactivity organizes the firing of neurons with related tuning to external variables, giving rise to robust population-based representations that are congruent with those of their participating neurons[14,16,17]. In addition, millisecond-timescale coactivity could also play a primary role in encoding information. That is, groups of neurons may encode a variable as a function of their joint activity regardless of whether each neuron is individually tuned to this variable. While this type of emergent coactivity-based coding has been described for physically well-defined variables, such as specific sensory inputs and actions[18–20], its possible cognitive function has not been explored.

Given the potential for rapid stabilization and retrieval of neural codes based on millisecond-timescale coactivity, such codes may support behavioral performance when animals must rapidly learn and flexibly retrieve salient information, a process we refer to here as 'dynamic memory'. Converging evidence suggests a prominent role of the hippocampus for such rapid and flexible learning[21–23], supporting models that frame the hippocampus as a fast learning system[24]. Moreover, neural activity in the hippocampus is organized into temporally precise coactivity patterns[15,22,25]. We therefore hypothesized that millisecond-timescale coactivity patterns in the hippocampus serve a primary role in encoding behaviorally relevant information supporting dynamic memory. To test this hypothesis, we developed a one-day, two-contingency discrimination task that we combined with multiunit recording of hippocampal CA1 neurons and causal optogenetic manipulation of intrahippocampal synapses. Our findings demonstrate a role for emergent coactivity-based representations in encoding contingency information and supporting dynamic memory retrieval.

Results

Mice learn and dynamically retrieve two new behavioral contingencies every day. We first established a one-day behavioral paradigm that recruits dynamic memory (Fig. 1). Mice were initially pretrained to collect a transiently available (5-s) drop of sucrose from a liquid dispenser after the presentation of an auditory cue (pretraining phase 1; Extended Data Fig. 1). Subsequently, animals experienced a new learning enclosure every day, which was defined by a new spatial topology, two new sets of wall-mounted LED displays and two newly positioned dispensers (pretraining phase 2; Extended Data Fig. 1). In this learning enclosure, animals encountered the following rule: immediately after tone presentation, one dispenser delivers a drop of sucrose solution, whereas the other dispenser simultaneously delivers a bitter (quinine) solution; both drops are transiently available. Importantly, the dispenser–solution pairing was contingent on which of the two sets of LED cues was illuminated concurrently with the tone (Fig. 1a,b). When animals reached an average of 80% performance in this pretraining

[1]Medical Research Council Brain Network Dynamics Unit, Nuffield Department of Clinical Neurosciences, University of Oxford, Oxford, UK. [2]Physiological Laboratory, Department of Physiology Development and Neuroscience, University of Cambridge, Cambridge, UK. [3]Department of Pharmacology, University of Oxford, Oxford, UK. ✉e-mail: mohamady.el-gaby@ndcn.ox.ac.uk; david.dupret@bndu.ox.ac.uk

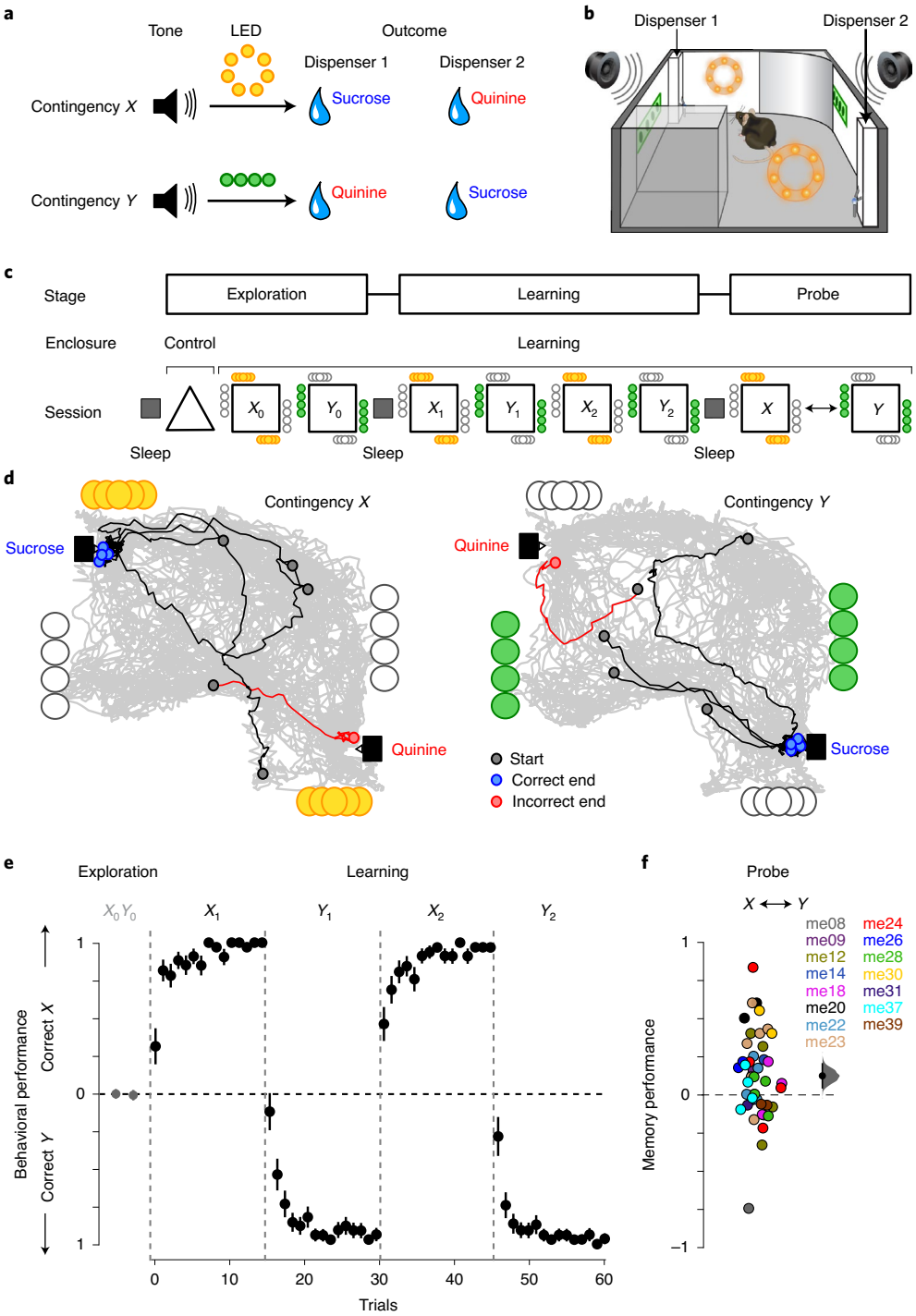

Fig. 1 | Mice rapidly acquire and flexibly retrieve a one-day two-contingency memory. a, The two-learning contingency layout. A tone signaled that both outcome dispensers delivered a liquid drop, the identity of which (sucrose versus quinine) depended on the active set of LEDs. **b**, Schematic of an example learning enclosure. **c**, The three-stage task structure. Tone-defined trials occurred in learning and probe sessions, with drop outcomes only delivered during learning. Sleep/rest sessions were recorded before and after exploration and after learning. **d**, Example animal paths during trials in contingency *X* and contingency *Y* (correct paths, black; incorrect paths, red), which are overlaid on the overall animal path (gray) for one learning session. Black and blue/red circles represent the path starting points and the correct/incorrect ending points, respectively. **e**, Behavioral performance for contingency-defined correct dispensers during exploration and learning ($n = 71$ d, 15 mice). For each learning trial, a score of 1 indicates that mice successfully identified the correct (sucrose-delivering) dispenser, while a score of –1 indicates that mice opted for the incorrect (quinine-delivering) dispenser; behavioral performance is reported as the mean score per trial number across days across mice (see Methods). Because the correct dispenser in one contingency (for example, *X*) was the incorrect dispenser in the other (for example, *Y*), behavioral performance is shown with respect to the current contingency, with the *y* axis ranging from 1 (correct *Y*), to 0 (chance) to 1 (correct *X*). **f**, Behavioral performance during the memory probe test showing that animals identified the correct dispenser for a given contingency (mean performance, 0.12 ± 0.04). Left, color-coded raw data points represent individual mice; right, effect size for the difference against zero computed from 1,000 bootstrapped resamples, with the black dot representing the mean, the black ticks representing 95% confidence intervals and the filled curve representing the resampled mean difference distribution.

phase, we then started the training phase, which included three stages every day (Fig. 1c). In the first stage, animals explored the new learning enclosure in two sessions, each with one of the two LED sets continuously illuminated, but without tone presentation or drop delivery, as well as another exploration session in a control (task-unrelated) enclosure ('exploration' stage; Fig. 1c and Extended Data Fig. 2a). In the second stage, animals learned to associate each LED set with the tone-triggered delivery of a selective drop outcome at each dispenser over four sessions alternating between active LEDs ('learning' stage; Fig. 1c). We refer to these associations as LED-defined behavioral 'contingencies' (*X* and *Y*; Fig. 1a), with animals learning two new contingencies every day (Extended Data Fig. 2b). During learning, mice rapidly developed a successful approach response to the correct (sucrose) dispenser over the incorrect (quinine) dispenser in each contingency (Fig. 1d,e and Extended Data Fig. 2b). In the final stage conducted at the end of each day (1 h after the end of learning), memory for the newly learned contingencies was tested in a probe session where the tone was presented without drop delivery while pseudorandomly switching between the two LED sets ('probe' stage; Fig. 1c). In these probe trials, mice continued to identify the correct dispenser (Fig. 1f and Extended Data Fig. 2c). Memory performance on a given day was unrelated to that on the previous day (Extended Data Fig. 3a) and held when averaging across all probe performances for each individual mouse (Extended Data Fig. 3b). Furthermore, while animals made more mistakes in the first probe trial following a switch in LEDs than in the other trials (Extended Data Fig. 3c), there was no deterioration of performance as the probe session progressed (Extended Data Fig. 3d). Thus, mice successfully learned to discriminate two new behavioral contingencies each day and flexibly retrieved a memory of this discrimination, providing a paradigm to study the neural substrates of dynamic memory.

Emergent millisecond-timescale coactivity discrimination of behavioral contingencies. To investigate whether an emergent coactivity code develops in our task, we monitored hippocampal CA1 neuronal ensembles during training days. We first trained a Bayesian classifier to decode the prevailing contingency on a trial-by-trial basis from the average firing rates of principal neurons and short-timescale (25-ms) pairwise temporal correlations between neuronal spike trains. Shuffling temporal correlations across trials while preserving trial-by-trial average firing rates markedly impaired decoding of the ongoing contingency (Fig. 2a and Extended Data Fig. 4a). Moreover, contingency information in temporal correlations alone was drastically impaired when shifting spikes to destroy short-timescale coactivity while maintaining correlations due to slow fluctuations of population firing rate in each trial (Fig. 2b). Short-timescale correlations also had significant explained variance for task contingencies (Fig. 2c). These results indicated the presence of contingency-related information in short-timescale coactivity beyond the information in single-neuron firing rates.

To investigate the task relevance of contingency-related coactivity, we isolated coactivity patterns nested within 25-ms time windows[26] separately in each contingency within the learning enclosure. We represented each pattern by a weight vector quantifying the contribution of each neuron to the coactivity underpinning that pattern (Fig. 2d). These coactivity patterns differed from those extracted in the control enclosure (Fig. 2e,f), showing their spatial context-selective expression. In addition, some learning enclosure patterns discriminated the two contingencies, being selective to either *X* or *Y* (Fig. 2e,f and Extended Data Fig. 4b). To investigate the functional significance of such patterns, we compared them to a matched group of learning enclosure patterns with high between-contingency similarity (Fig. 2e,f and Extended Data Fig. 4b). We refer to these as contingency-discriminating and contingency-invariant coactivity patterns, respectively. Neurons that contributed the most to a given pattern are henceforth referred to as 'members' of that pattern (see Methods).

We confirmed that members of the same contingency-discriminating, but not invariant, pattern were more correlated in one contingency than the other (Fig. 3a). Importantly, however, members of contingency-discriminating patterns were not individually contingency selective (Fig. 3b and Extended Data Fig. 4c) regardless of the membership threshold used (Extended Data Fig. 4d,e) and are hence separable from previously reported contextually modulated neurons[27–29]. Moreover, such coactivity-based contingency discrimination was not explained by differences in temporal firing properties of individual member neurons between contingencies (Fig. 3c–e). Furthermore, contingency-discriminating pattern members were not tuned to goal locations (Fig. 3f,g) and hence did not report trajectories to goals[30]. We also noted no differences in the participation of neurons along the transverse axis of the CA1 to contingency-discriminating and invariant patterns

Fig. 2 | CA1 coactivity-based discrimination of task contingencies. a, Data analysis with a bootstrap-coupled estimation (DABEST) plot[50] used to visualize the effect size of a Gaussian naive Bayesian classifier decoding contingencies during learning using a combination of CA1 principal neuron firing rates and pairwise correlations. Top: raw data points for individual days (mean accuracy: actual = 66.5% ± 2.9%, shuffled correlations = 55.1% ± 1.7%, shuffled rates = 62.0% ± 2.5% and both shuffled = 48.3% ± 0.2%; *N* = 23 d from 10 mice). Bottom: effect size for the difference with respect to the left-most group (that is, 'actual') computed from 1,000 bootstrapped resamples; black dot, paired mean difference; black ticks, 95% confidence intervals; filled curve, resampled paired mean difference distribution. DABEST plots are used from here onward (see Methods section "Statistics"). **b**, Decoding accuracy using 25-ms correlations compared to that with spikes shifted to maintain correlations due to slow population dynamics but destroy short-timescale coactivity (mean accuracy: actual = 62.8% ± 2.6% and shifted spikes = 50.8% ± 2.2%; *N* = 23 recording days). **c**, Explained variance for contingency using trial-by-trial pairwise correlations among all CA1 principal neurons compared to shuffled pairwise correlations (mean explained variance: actual = 0.028 ± 0.000% and shuffled = 0.020 ± 0.000%; *N* = 19,852 neuron pairs; Wilcoxon test (two-sided), *Z* = 96651960.0 and *P* = 0.02). **d**, Example CA1 coactivity patterns detected in one learning session. Each pattern is represented as a vector containing the contribution (weight) of each neuron's spiking to the coactivity defining that pattern[26]. For each pattern, neurons with a weight above 2 s.d. of the mean were referred to as members (color coded). Shown is an example raster plot of the spike trains (top left, one neuron per row) along with the coactivity strength of one (dark blue) pattern over time (bottom left) and the vectors (right) of other coexisting patterns. Projecting such vectors onto neuron spike trains allowed tracking of the time course of each pattern's strength (for example, bottom left dark blue time course of coactivity peaks for the left-most vector, with the member spiking shown in dark blue on the raster plot above; AU, arbitrary units). **e**, Example similarity matrices of patterns detected in the learning enclosure with contingency *Y* compared to patterns detected in sessions with the same contingency (within-contingency, left) or the other contingency (between-contingency, middle) or to patterns detected in the control enclosure (between-enclosure, right). **f**, Cosine similarity for contingency-discriminating and contingency-invariant patterns across conditions; contingency-discriminating: within-contingency = 0.60 ± 0.02, between-contingency = 0.46 ± 0.01 and between-enclosure = 0.37 ± 0.02; contingency-invariant: within-contingency = 0.80 ± 0.02, between-contingency = 0.87 ± 0.01 and between-enclosure = 0.44 ± 0.02.

(52.1% and 48.2% of pattern member neurons found in the proximal and distal CA1, respectively; Fisher's exact test, odds ratio = 1.17 and $P = 0.55$), no segregation by hemisphere (Extended Data Fig. 4f) and no differences in the participation of neurons from the deep or superficial CA1 pyramidal sublayer to contingency-discriminating compared to contingency-invariant patterns (39.9% and 28.4% of pattern member neurons, respectively; Fisher's exact test, odds ratio = 1.44 and $P = 0.20$). However, we observed a trend toward contingency-discriminating coactivity pattern members firing at earlier theta phases compared to members of contingency-invariant patterns (Extended Data Fig. 4g). Overall, these findings identify an emergent, short-timescale neural coactivity-based discrimination of behavioral contingencies in the hippocampal CA1.

We next asked whether contingency-discriminating coactivity patterns relate to contingency learning. When we tracked the strength of each pattern (Fig. 2d) over time, we found that contingency-invariant patterns began increasing in strength during the initial exploration of the new learning enclosure on each day before animals experienced task contingencies; their strength further increased and subsequently plateaued during learning (Fig. 4a and

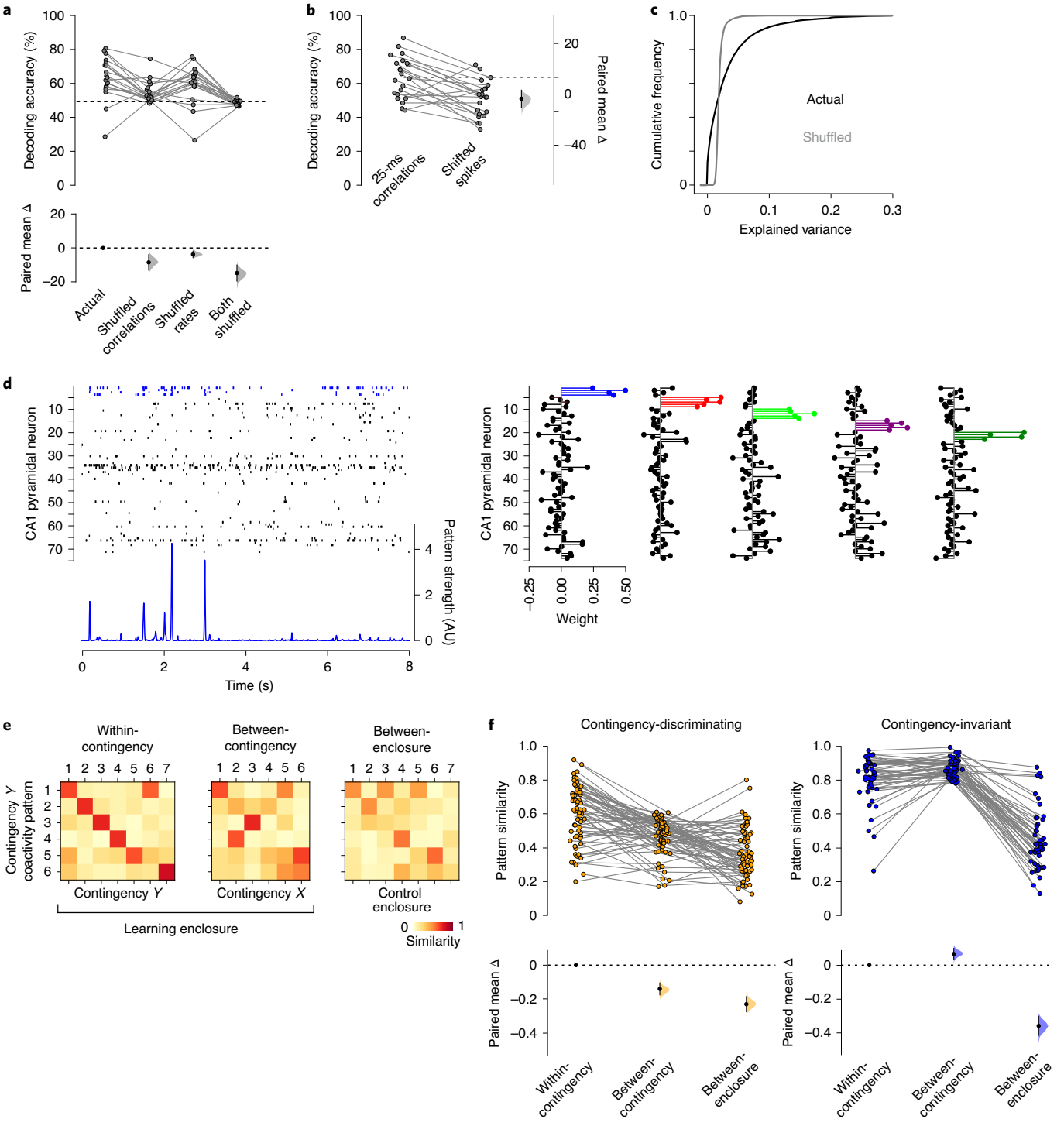

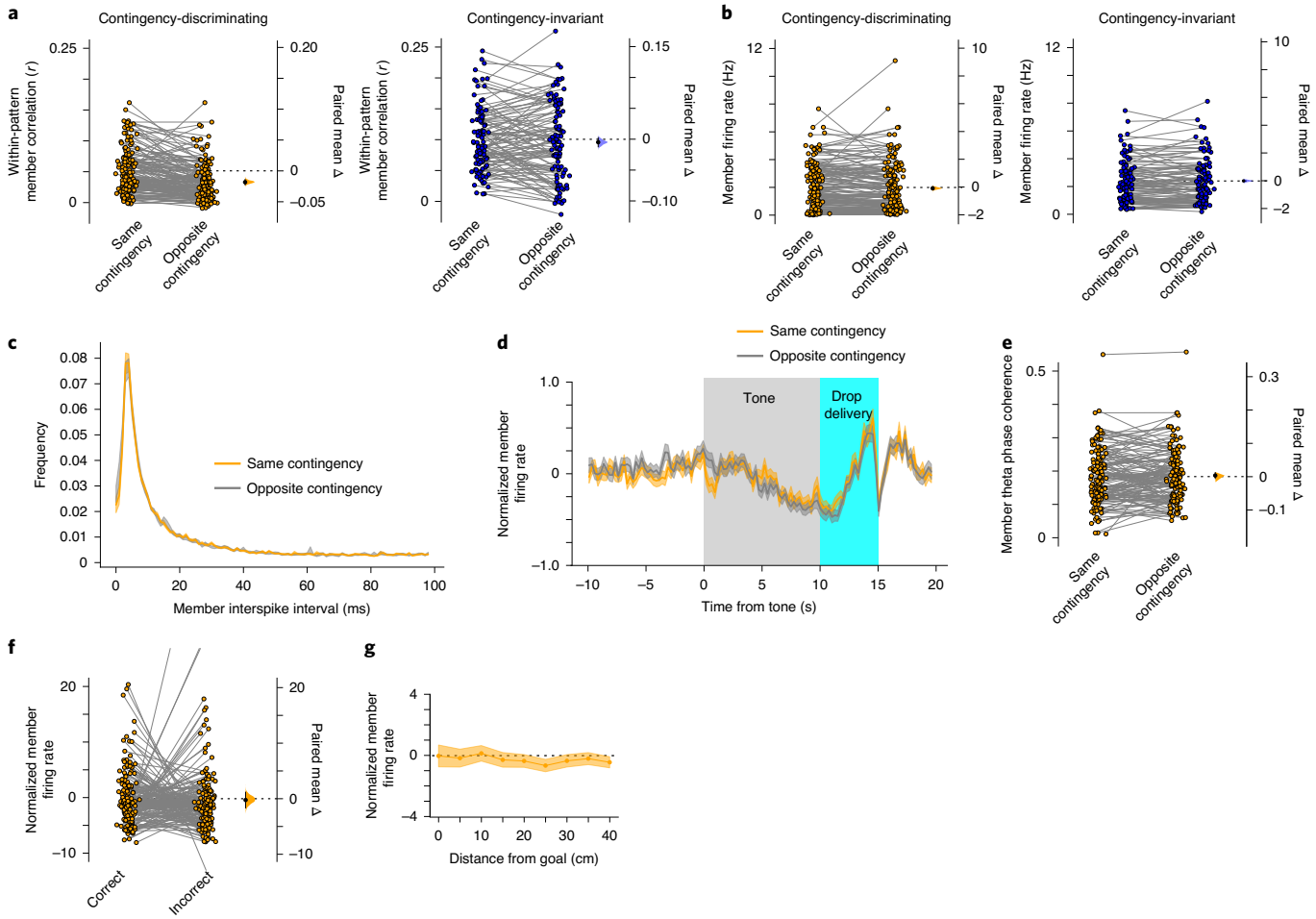

Fig. 3 | Discrimination of task contingencies is an emergent property of neural coactivity. a, Mean temporal correlations among members of a given contingency-invariant and contingency-discriminating pattern in the same contingency (that is, the contingency in which the patterns were detected) and the opposite contingency. The following mean Pearson correlation values were obtained: contingency-invariant members, same contingency = 0.100 ± 0.005 and opposite contingency = 0.096 ± 0.006; contingency-discriminating members, same contingency = 0.052 ± 0.003 and opposite contingency = 0.033 ± 0.002. **b**, Mean firing rates of contingency-discriminating and contingency-invariant members; contingency-discriminating, same contingency = 2.06 ± 0.14 Hz and opposite contingency = 1.93 ± 0.15 Hz; contingency-invariant, same contingency = 2.28 ± 0.15 Hz and opposite contingency = 2.31 ± 0.15 Hz. **c**, Interspike intervals of contingency-discriminating pattern member neurons in the same contingency and the opposite contingency (two-way repeated-measures ANOVA; no main effect of contingency, $F(1) = 0.549$, $P = 0.458$, $\eta^2 = 8 \times 10^{-6}$; main effect of interval, $F(98) = 373.0$, $P = 0.000$, $\eta^2 = 0.520$; no contingency: interval interaction, $F(98) = 0.738$, $P = 0.976$, $\eta^2 = 0.001$). **d**, *Z*-scored firing rates during tone and drop delivery of contingency-discriminating pattern member neurons in the same contingency and the opposite contingency (two-way repeated-measures ANOVA; no main effect of contingency, $F(1) = 4.97 \times 10^{-25}$, $P = 1.00$, $\eta^2 = 1.19 \times 10^{-29}$; main effect of time, $F(117) = 14.4$, $P = 2.52 \times 10^{-269}$, $\eta^2 = 0.040$; no contingency:time interaction, $F(117) = 0.92$, $P = 0.716$, $\eta^2 = 0.003$). **e**, Spike-phase coherence to theta oscillations of contingency-discriminating pattern member neurons is indistinguishable across contingencies; mean coherence, same contingency = 0.186 ± 0.007 and opposite contingency = 0.188 ± 0.007. Similarly, the theta phase preference of contingency-discriminating neuron firing is indistinguishable across contingencies (mean theta phase preference with respect to theta peak, same contingency = 156 ± 6° and opposite contingency = 146 ± 6°; Watson–Wheeler test, $W(2) = 0.44$ and $P = 0.801$). **f**,**g**, Contingency-discriminating pattern member firing rates (*z* scored) are indistinguishable at correct and incorrect dispensers (**f**) (normalized mean, correct = −0.2 ± 0.4 and incorrect = −0.4 ± 0.5) and are not modulated by distance from goal location (**g**). Linear regression of rate against distance from sucrose dispenser; $r = -0.02$ and $P = 0.41$.

Extended Data Fig. 5a,b). Conversely, contingency-discriminating coactivity was more stable during exploration but markedly increased during contingency learning (Fig. 4a and Extended Data Fig. 5a,b). Pattern strengthening during learning reflected increased temporal correlations between members' activity rather than changes in their average firing rates (Extended Data Fig. 5c,d). Furthermore, the cofiring of contingency-invariant pattern members increased during sharp-wave/ripples (SWRs) in post-exploration compared to pre-exploration sleep and increased again in the sleep session after learning, while contingency-discriminating pattern members only increased their SWR cofiring after contingency learning (Fig. 4b,c). Thus, the distinction between contingency-invariant and contingency-discriminating pattern members was not equivalent to the difference between the previously described 'rigid' and 'plastic' cells[31]. Moreover, our findings did not simply reflect representations of rewarded/aversive locations[27] because pattern strength was calculated outside of dispenser locations, nor were these findings a simple reflection of the animal's differential behavior across the two contingencies (that is, heading toward a given dispenser; Extended Data Fig. 5e). Importantly, the reinstatement

of contingency-discriminating patterns during memory retrieval predicted trial-by-trial performance; these patterns were stronger before correct behavioral responses than before incorrect behavioral responses to tone presentation (Fig. 4d and Extended Data Fig. 5f). This contingency-selective and performance-related reinstatement of CA1 coactivity was not associated with a firing rate bias of member neurons or animal running speed (Extended Data Fig. 5g,h) and was notably absent when animals performed at chance (that is, when correct and incorrect trials were equivalent; Extended Data Fig. 5i). By contrast, the strength of contingency-invariant patterns was not related to trial-by-trial memory performance (Fig. 4d). Moreover, while there was contingency-related information in longer (1-s) timescale coactivity (Extended Data Fig. 5j), the reinstatement of second-timescale contingency-discriminating coactivity during the probe session did not predict memory performance (Extended Data Fig. 5k). These findings show that CA1 neuronal spiking is gradually organized during learning to form millisecond-timescale coactivity patterns representing newly learned contingencies, which are subsequently reinstated on a trial-by-trial basis during dynamic memory retrieval.

Distinct spatial tuning of contingency-discriminating and invariant coactivity patterns. During exploration of a new environment, CA1 neurons with overlapping place fields can form spatially tuned coactivity patterns[17,32]. To investigate the spatial tuning of coactivity patterns during contingency learning, we computed for each detected pattern the spatial map corresponding to the time course of its activation strength as well as the individual firing rate maps of each of its member neurons. Contingency-discriminating coactivity was markedly less spatially coherent than contingency-invariant coactivity (Fig. 5a–d and Extended Data Fig. 6). This was concomitant with the less spatially coherent firing of contingency-discriminating pattern members than their contingency-invariant counterparts (Extended Data Fig. 7a,b), with contingency-discriminating members also exhibiting a trend toward more place fields within a given session than contingency-invariant members (Extended Data Fig. 7c). Moreover, while members of a given contingency-invariant pattern had overlapping firing fields, members of a given contingency-discriminating pattern were markedly less spatially correlated (Fig. 5a,b,e and Extended Data Fig. 6). This weaker spatial overlap was observed regardless of the membership threshold used (Extended Data Fig. 7d,e) and was robust to differences in temporal correlation among members' spike trains (Extended Data Fig. 7f). In addition, while contingency-invariant coactivity was spatially biased toward the place fields of their member neurons, this bias was significantly weaker for contingency-discriminating patterns (Extended Data Fig. 7g,h). This finding was corroborated by a separate analysis showing lower place field similarity of neuron pairs with high explained variance for contingency than neuron pairs with low explained variance (Extended Data Fig. 7i). Finally, we found no evidence that contingency discrimination by a given

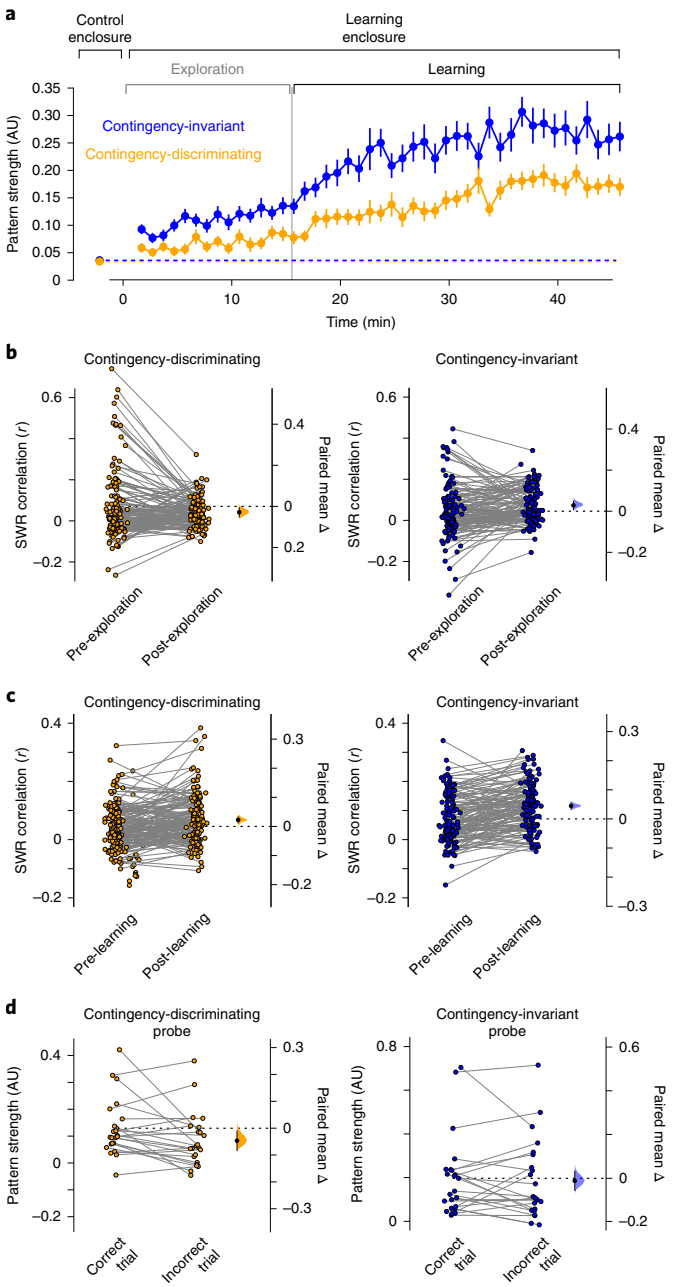

Fig. 4 | Contingency-discriminating patterns develop with learning and predict probe performance. a, Time course of pattern strength. Contingency *X*-discriminating and contingency *Y*-discriminating patterns were pooled, and the coactivity strength of each pattern was quantified in exploration/learning sessions of its preferred contingency. Dashed lines represent mean pattern strength in the control enclosure. Linear regression of strength against time during exploration (contingency-invariant, $r = 0.17$ and $P = 4.22 \times 10^{-6}$; contingency-discriminating, $r = 0.09$ and $P = 0.003$) and learning (contingency-invariant, $r = 0.15$ and $P = 2.17 \times 10^{-8}$; contingency-discriminating, $r = 0.19$ and $P = 1.80 \times 10^{-17}$). Slopes of contingency-invariant patterns were steeper than those of contingency-discriminating patterns during exploration (slope = 0.0036 ± 0.0007 and 0.0019 ± 0.0006 units per min, respectively; Mann–Whitney *U*-test (two-sided), $U = 1279.0$ and $P = 0.03$), but not during learning (slope = 0.0032 ± 0.0009 and 0.0032 ± 0.0005 units per min, respectively; Mann–Whitney *U*-test (two-sided), $U = 1441.0$ and $P = 0.21$). Error bars represent s.e.m. across patterns. **b**,**c**, Contingency-discriminating and contingency-invariant pattern member correlations during SWRs in sleep before and after exploration (**b**) and before and after contingency learning (**c**). The mean SWR correlation for contingency-invariant members was 0.045 ± 0.012 during pre-exploration, 0.071 ± 0.008 during post-exploration (pre-learning) and 0.116 ± 0.007 during post-learning. The mean SWR correlation for contingency-discriminating members was 0.070 ± 0.015 during pre-exploration, 0.045 ± 0.006 during post-exploration (pre-learning) and 0.068 ± 0.007 during post-learning. **d**, Mean pattern strength before an animal's choice during probe trials in sessions where animals performed above chance; contingency-discriminating, correct = 0.13 ± 0.02 and incorrect = 0.08 ± 0.02; contingency-invariant, correct = 0.20 ± 0.04 and incorrect = 0.19 ± 0.04.

coactivity pattern reflects contingency-gated spatial remapping of its member neurons. In fact, the spatial map of an individual member of either pattern type was on average more similar across sessions of different contingencies than sessions of the same contingency (Fig. 5f,g and Extended Data Fig. 7j), even when matching the spatial coherence of contingency-discriminating pattern members to that of their contingency-invariant counterparts (Extended Data Fig. 7k). Moreover, members of the same contingency-discriminating pattern were as spatially correlated with each other across sessions of their preferred contingency as they were across sessions of the opposite contingency (Extended Data Fig. 7l). Overall, these findings show that contingency-invariant coactivity provides robust place representations by binding spatially congruent neurons. By contrast, contingency-discriminating patterns stitch together neurons irrespective of their spatially correlated activity, giving rise to spatially discontiguous coactivity consistent with a specialization in representing ongoing behavioral contingency.

$CA3^L \rightarrow CA1$ inputs are necessary for contingency-discriminating coactivity and dynamic memory retrieval. Finally, to address the functional role of contingency-discriminating coactivity, we sought to identify and manipulate a neural pathway necessary for their formation. CA1 coactivity could rely on synaptic inputs from the recurrently connected upstream hippocampal CA3 area[33,34], and recent work suggests a critical mnemonic role of left CA3 ($CA3^L$) inputs to the CA1 (refs. [35,36]). Accordingly, we transduced $CA3^L$ pyramidal neurons of Grik4-Cre mice with the yellow light-driven proton pump Archaerhodopsin-3.0 (Fig. 6a,b); bilateral implantation of tetrodes and optic fibers further allowed for the simultaneous monitoring of, and light delivery to, CA1 ensembles. Light delivery targeting $CA3^L$ axons in the CA1 during learning markedly reduced the power of theta-nested slow-gamma, but not mid-gamma, oscillations in the CA1 (Fig. 6c and Extended Data Fig. 8a–c), consistent with the suggestion that CA1 slow-gamma oscillations report incoming CA3 inputs[37,38]. While suppressing $CA3^L \rightarrow CA1$ inputs preserved both the organization of CA1 neurons into coactivity patterns during learning and the reinstatement strength of such patterns during memory retrieval (Extended Data Fig. 8d,e), this intervention altered the information content of CA1 coactivity. First, the distribution of between-contingency pattern similarity and pattern strength ratio was shifted toward contingency invariance (Fig. 6d,e and Extended Data Figs. 8f and 9). Second, this manipulation reduced the explained variance for contingencies in short-timescale pairwise correlations (Extended Data Fig. 8g). Third, Bayesian decoding of contingencies using such short-timescale coactivity was markedly impaired

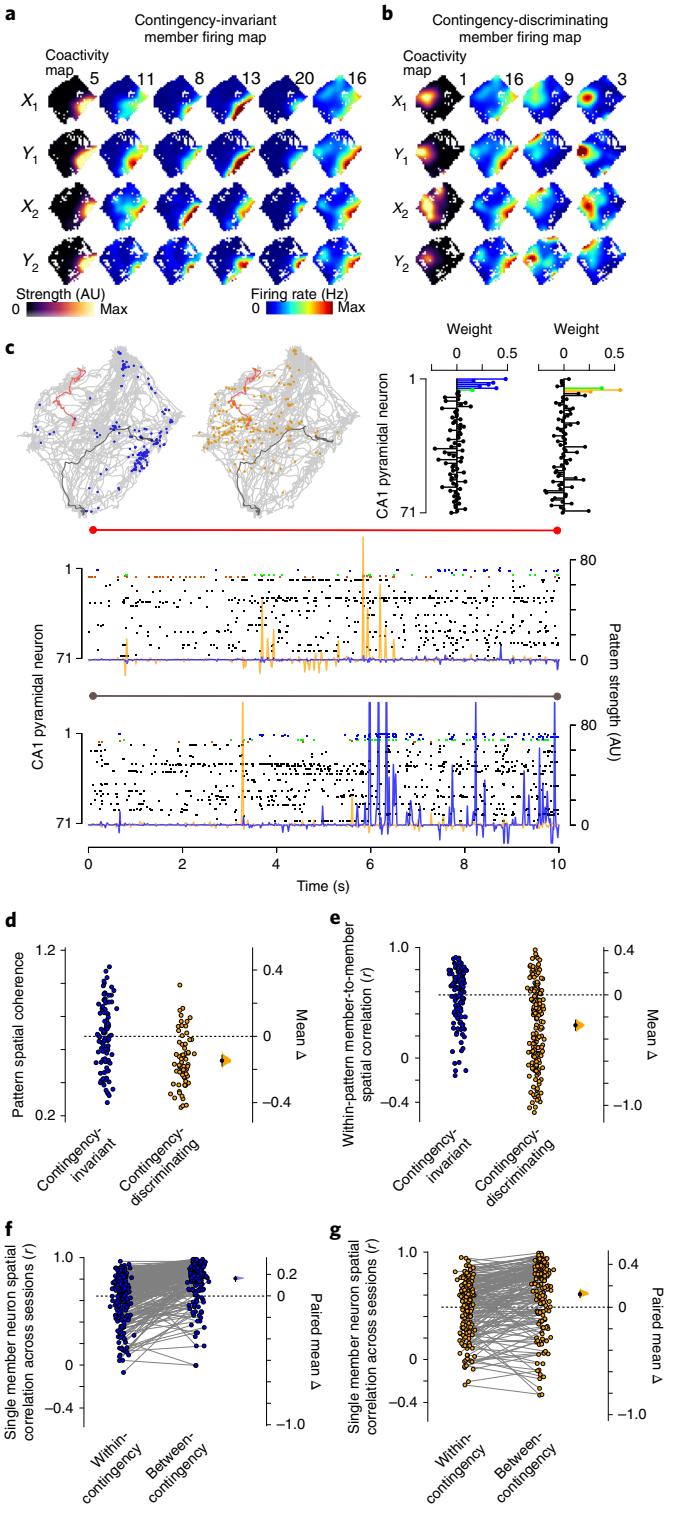

Fig. 5 | Contingency-discriminating CA1 coactivity is spatially discontiguous. a,**b**, Example coactivity strength maps and corresponding firing rate maps of individual members for a contingency-invariant (**a**) and a concomitantly recorded contingency-discriminating (**b**) pattern across all sessions. Note that the right-most member of the contingency-invariant pattern is also a member of the contingency-discriminating pattern. Maximum firing rate (in Hz) or maximum coactivity strength (AU) are shown above each firing rate map or pattern strength map, respectively. **c**, Principal neuron spike trains and coactivations along two animals' paths (red and charcoal) for the contingency-invariant (blue) and contingency-discriminating (orange) patterns shown in **a** and **b**. Members are indicated by the color-coded assembly weight vectors and spike times in the raster plots (note the shared member is indicated in green). The line above each raster is color coded as in the path plots. **d**, Contingency-discriminating coactivity is less spatially coherent than that of contingency-invariant patterns (mean spatial coherence, contingency-invariant = 0.64 ± 0.02 and contingency-discriminating = 0.51 ± 0.02). **e**, Contingency-discriminating member neuron firing fields are less spatially overlapping (mean spatial correlation, contingency-invariant = 0.57 ± 0.02 and contingency-discriminating = 0.30 ± 0.03). **f**,**g**, Spatial correlation of individual contingency-invariant (**f**) and contingency-discriminating (**g**) pattern members across sessions of the same (within) contingency or opposite (between) contingencies (mean spatial correlation: contingency-invariant, within-contingency = 0.64 ± 0.01 and between-contingency = 0.80 ± 0.01; contingency-discriminating, within-contingency = 0.49 ± 0.02 and between-contingency = 0.61 ± 0.02).

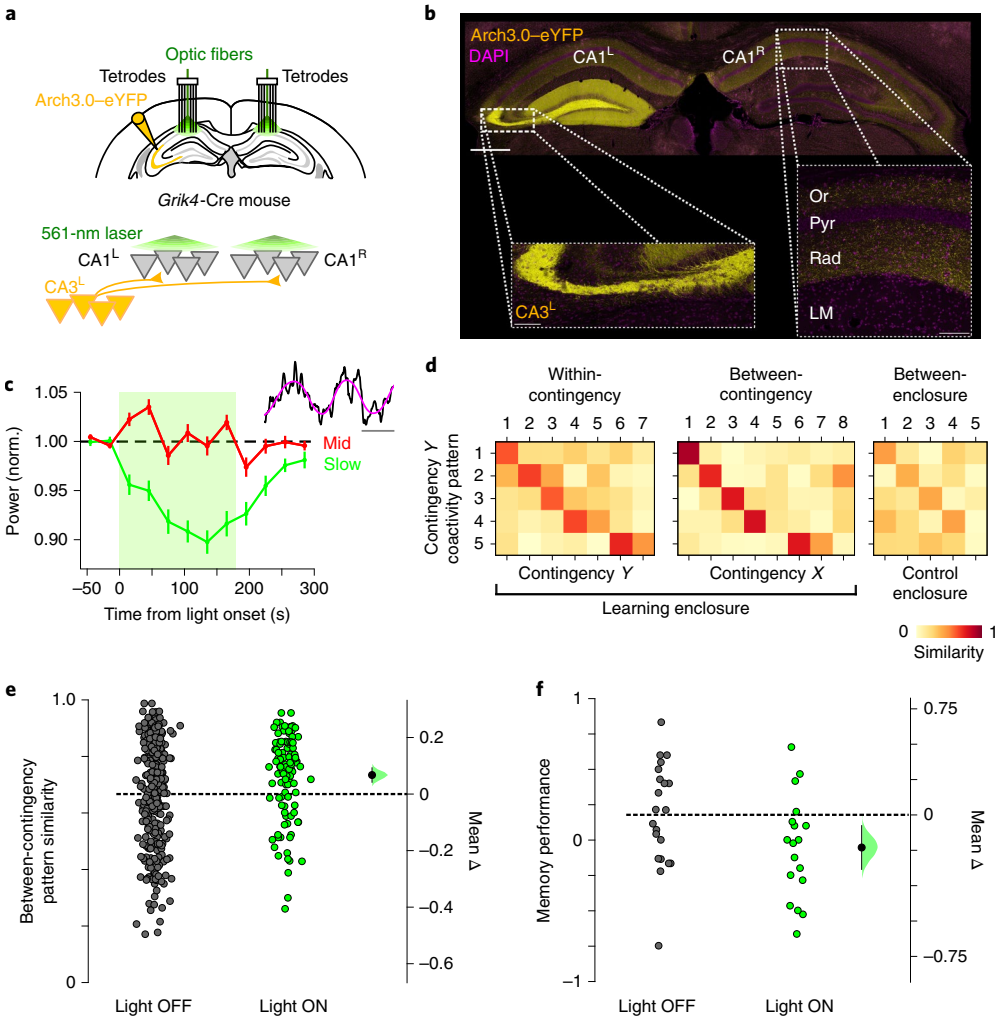

Fig. 6 | Contingency-discriminating CA1 coactivity requires CA3^{L} inputs and supports dynamic memory retrieval. a, CA3^{L} → CA1 optogenetic suppression protocol. CA3^{L} neurons were transduced with Archaerhodopsin-3.0 (Arch3.0) in Grik4-Cre mice ($n = 5$), and their axonal projections in the CA1 were targeted bilaterally during learning with yellow 561-nm light delivery from implanted optic fibers; 12 tetrodes monitored CA1 neurons. **b**, Expression of Arch3.0–eYFP in the somata of CA3^{L} neurons and their axons in the CA1 bilaterally (top); nuclei are stained with DAPI. Higher-magnification images of eYFP-expressing CA3 neurons (bottom left) and their axons in the contralateral CA1 (bottom right). Representative images from five animals; scale bars, top = 100 μm and bottom = 10 μm; stratum: Or, oriens; Pyr, pyramidale; Rad, radiatum; LM, lacunosum moleculare. **c**, Light delivery to Arch3.0-expressing CA3^{L} axons reduced the power of theta-nested slow-gamma, but not mid-gamma, oscillations in the CA1 (Wilcoxon test (two-sided): slow-gamma, $Z = 8.0$ and $P = 9.78 \times 10^{-8}$; mid-gamma, $Z = 291.0$ and $P = 0.167$). Inset shows an example raw trace of two theta cycles nesting strong mid-gamma (~50–90 Hz) and slow-gamma (~25–40 Hz) oscillations, respectively; raw trace and theta component are represented in black and magenta, respectively; scale bar, 100 ms. **d**, Example similarity matrices of patterns detected in the learning enclosure during CA3^{L} → CA1 input suppression with contingency *Y* compared to patterns detected in subsequent sessions with the same contingency (within-contingency, left) or the other contingency (between-contingency, middle) or to patterns detected in the control enclosure (between-enclosure, right). **e**, CA3^{L} → CA1 input suppression shifted the between-contingency similarity of CA1 patterns toward contingency invariance; $n = 54$ and 57 patterns detected in contingency *X* and contingency *Y*, respectively, on days with CA3^{L} → CA1 input suppression (light ON days); mean between-contingency cosine similarity, light OFF = 0.65 ± 0.01 and light ON = 0.74 ± 0.01. **f**, CA3^{L} → CA1 input suppression during learning impaired subsequent probe trial performance (mean performance, light OFF days = 0.18 ± 0.08 and light ON days = –0.05 ± 0.09). All error bars represent mean ± s.e.m. except when used with Gardner–Altman DABEST plots, where they represent mean difference (or paired mean as indicated) ±95% confidence intervals.

with CA3^{L} → CA1 input suppression (Extended Data Fig. 8h). At the behavioral level, suppressing CA3^{L} → CA1 inputs selectively during learning had no effect on ongoing performance (Extended Data Fig. 8i), but reduced memory performance to chance levels in the subsequent probe test 1 h after learning, during which there was no input suppression (Fig. 6f). This latent memory impairment was seen when mice had to flexibly retrieve two contingencies (Fig. 6f and Extended Data Fig. 8j–l), but not when retrieving only one contingency (Extended Data Fig. 8m). Moreover, flexible memory retrieval of the two contingencies was preserved after suppressing right CA3 inputs to the CA1 (Extended Data Fig. 8n–u). Together, these findings show that short-timescale CA1 coactivity-based contingency information necessitates CA3^{L} inputs and is required for the dynamic retrieval of two-contingency memory.

Discussion

In this study, we report a coactivity-based hippocampal code for dynamic memory retrieval of short-lived behavioral contingencies.

Encoding information as an emergent property of coactivity among multiple neurons (Extended Data Fig. 10a) allows for the effective discrimination of newly encountered contingencies every day without committing individual neurons to represent such short-lived cognitive variables. The emergent nature of this code points to short-timescale coactivity as a primary feature of neural activity that is used to encode information and guide cognition rather than only playing secondary roles, such as organizing or stabilizing single-neuron rate-based codes. In particular, our findings show that millisecond-timescale coactivity is highly suited for mnemonic processing of short-lived information; it is rapidly formed and readily reinstated to support flexible memory retrieval. Millisecond-timescale neural coactivity may preferentially exhibit STDP[11,12,39] to rapidly stabilize the code in memory. By contrast, while second-timescale coactivity contained contingency information in our task, its reinstatement during dynamic memory retrieval was not predictive of trial-by-trial performance. Second-timescale coactivity may exhibit slower plasticity and may hence be more suited for stable representation of long-lived contingencies.

Our findings also provide new insights into the role of correlated neural activity in guiding contextual behavior. Spatial remapping, where patterns of spatial correlations between hippocampal principal cells disambiguate distinct spatial contexts, has been proposed as a neural basis for contextual learning[23]. In this study, we observed that contingency-discriminating coactivity is not a reflection of spatial remapping. Instead, our findings are consistent with the view that spatial remapping may be a specific instance of a more general phenomenon of 'temporal remapping', in which the short-timescale temporal correlation structure of neurons differs across distinct contexts[23]. Indeed, in tasks where animals must disambiguate different spatial reference frames, millisecond-timescale coactivity is a robust correlate of moment-by-moment behavioral discrimination of different contexts, both in networks that show spatial remapping[22] and in those that do not[25]. This is also consistent with a reader-centric view of neural codes[5], because downstream reader/actuator neurons can detect temporal but not spatial correlations among their input neurons. Notably, one prediction from this coding scheme is that downstream receiver neurons 'read' the incoming information, represented as an emergent property of the collective activity of multiple neurons, by disambiguating the relevant patterns of millisecond input coincidence from the myriad of other inputs they receive[5]. Such decoding may be implemented by a 'reader' network[40] or even a single reader neuron[41] (see also Extended Data Fig. 10b).

Our findings further establish that to 'write' a millisecond coactivity code for learned contingencies in memory, $CA3^{L} \rightarrow CA1$ inputs are necessary. Whether this is related to lateralization in information content, processing and/or plasticity[35,42] of $CA3 \rightarrow CA1$ inputs remains to be investigated. Nevertheless, we show that distinct types of coactivity patterns show qualitatively distinct functional plasticity. While contingency-invariant patterns develop during exploration and are reactivated in SWRs during offline (sleep/rest) periods following spatial exploration, contingency-discriminating patterns show robust increases in strength during learning and are reactivated offline in SWRs after contingency learning. Thus, both invariant and discriminating patterns show a signature of previously described plastic cells[31], albeit in different behavioral stages. This is consistent with a division of labor among hippocampal coactivity patterns, with contingency-invariant patterns reflecting unsupervised learning about the spatial structure of the environment and contingency-discriminating patterns supporting flexible memory-guided behavior. Altogether, our findings open new perspectives for future empirical and modeling studies to elucidate the mechanisms for writing and reading coactivity-based information and to relate coding schemes across multiple timescales of population activity.

How can the code be written and read? The hippocampus is embedded in a wider network of cortical and subcortical structures that may mediate or modulate the formation of the emergent coactivity code we describe here (writing) and its subsequent use by downstream neurons (reading) to select contingency-specific behavior. Below we outline hypotheses about possible mechanisms for both writing and reading processes.

We show a necessity of $CA3^{L} \rightarrow CA1$ inputs during learning for the expression of an emergent coactivity code for short-lived behavioral contingencies, which opens a window into the generative mechanisms at play. Left hemisphere-originating CA3 inputs in mice exhibit more robust long-term plasticity[35,42], including STDP[42], and are preferentially involved in long-term memory compared to right CA3 inputs[35,36]. Such a difference in plasticity may provide part of the mechanism by which contingency-discriminating patterns are strengthened during learning. The dynamic memory task we assess here necessitates the rapid acquisition and stabilization of contingency information (within 30 trials in each contingency across ~3 h) as well as its rapid and flexible retrieval in the memory probe test (1 h after learning, with frequent pseudorandom switches in contingency). Such rapid mnemonic processing may be preferentially coded by short-timescale coactivity, because STDP mechanisms are more likely to rapidly stabilize neuronal cofiring within shorter (tens of milliseconds) windows than within longer (1-s) windows[11,12,39]. Indeed, we show that shorter-timescale (25-ms) but not longer-timescale (1-s) coactivity is reinstated to predict performance (Fig. 4d and Extended Data Fig. 5k). However, it is also possible that other plasticity mechanisms are at play (including non-synaptic ones). While STDP might stabilize millisecond-timescale coactivity patterns, what processes generate such contingency-discriminating coactivity in the first place? Neurons in the dentate gyrus, two synapses upstream of the CA1, have been implicated in pattern separation processes that may be necessary for contextual behavior[43] and can do so through differences in millisecond-timescale coactivity[25]. Moreover, there is evidence for a left dominance in the expression of the activity marker cFos in the dentate gyrus during novel object exploration[44]. Importantly, while CA3 neurons in one hemisphere send commissural projections to the contralateral hemisphere[33], the two hemispheres seem to retain functional differences in their projections to the CA1 (refs. [35,42]), which we target directly. Such lateralization could, in part, result from a developmental lateralization of factors involved in activity and plasticity[45], which may be robust to any potential synchronizing effects of commissural projections. Therefore, it is plausible that a combination of lateralized processing of contextual information, starting as early as the pattern separation circuits of the dentate gyrus, and lateralized plasticity at $CA3 \rightarrow CA1$ synapses contribute to the formation and stabilization of emergent contingency-discriminating patterns in the CA1, respectively. Given that contingency-discriminating patterns emerge during learning rather than spatial exploration (Fig. 4a), their formation is not simply a reflection of sensory differences between the two LED displays (which are also distinct during exploration sessions X_0 and Y_0), but instead relates to the different reward contingencies the animal must learn to discriminate. Indeed, recent evidence suggests that neural discrimination of distinct spatial contexts in the CA1, but not the dentate gyrus, is related to behavioral discrimination of these contexts[46], suggesting an additional gating of behaviorally relevant environmental differences between the dentate gyrus and CA1. How such behavioral contingency information is conveyed to the CA1 is currently unclear and may involve inputs from the prefrontal cortex[47]. The finding described here that an emergent coactivity code in the hippocampal CA1 is necessary for the dynamic retrieval of contingency discrimination will motivate subsequent empirical and modeling studies that elucidate the cross-circuit interactions involved in generating such functional coactivity.

How is the hippocampal coactivity code for contingencies decoded by downstream neurons in executive and motor areas to elicit appropriate behaviors in each contingency? Cortical neurons have membrane time constants in the range of 10–30 ms (ref. [9]), meaning that convergent input from neurons coactive at the 25-ms timescale we investigated here can exhibit effective temporal summation in the downstream (reader) neuron's dendrites and contribute to its spiking. Moreover, coincident synaptic activation within this time window is consistent with the initiation of active voltage-gated conductances in dendrites, which allows for their supralinear summation[48]. This may also serve as a mechanism for disambiguating different patterns of coactivity by a single reader neuron, where inputs that are preferentially spatially clustered on individual dendrites will be more likely to elicit such non-linearities than more dispersed inputs[49], even when the mean synaptic weights of such inputs are indistinguishable (Extended Data Fig. 10b). This would allow for the selective reading of emergent coactivity, as reader neurons would not disambiguate the firing of individual members of contingency-discriminating coactivity patterns, only their synchronous activity. Other single-neuron and network-based coactivity reading mechanisms have also been suggested[40,41]. For all of these cases, the fast (tens of milliseconds) nature of this code should allow for the quick processing of contingency information, supporting rapid behavioral responses in dynamically changing environments. These outlined candidate mechanisms by which emergent coactivity codes could be read by downstream circuits may be tested in future ex vivo, in vivo and in silico studies.

Online content

Any methods, additional references, Nature Research reporting summaries, source data, extended data, supplementary information, acknowledgements, peer review information; details of author contributions and competing interests; and statements of data and code availability are available at https://doi.org/10.1038/s41593-021-00820-w.

Received: 19 June 2020; Accepted: 18 February 2021;
Published online: 29 March 2021

References

1. Adrian, E. D. The impulses produced by sensory nerve endings: part I. *J. Physiol.* **61**, 49–72 (1926).
2. O'Keefe, J. & Dostrovsky, J. The hippocampus as a spatial map. Preliminary evidence from unit activity in the freely-moving rat. *Brain Res.* **34**, 171–175 (1971).
3. Optican, L. M. & Richmond, B. J. Temporal encoding of two-dimensional patterns by single units in primate inferior temporal cortex. III. Information theoretic analysis. *J. Neurophysiol.* **57**, 162–178 (1987).
4. O'Keefe, J. & Recce, M. L. Phase relationship between hippocampal place units and the EEG theta rhythm. *Hippocampus* **3**, 317–330 (1993).
5. Buzsáki, G. Neural syntax: cell assemblies, synapsembles, and readers. *Neuron* **68**, 362–385 (2010).
6. Churchland, M. M. et al. Neural population dynamics during reaching. *Nature* **487**, 51–56 (2012).
7. Mante, V., Sussillo, D., Shenoy, K. V. & Newsome, W. T. Context-dependent computation by recurrent dynamics in prefrontal cortex. *Nature* **503**, 78–84 (2013).
8. Yuste, R. From the neuron doctrine to neural networks. *Nat. Rev. Neurosci.* **16**, 487–497 (2015).
9. Koch, C., Rapp, M. & Segev, I. A brief history of time (constants). *Cereb. Cortex* **6**, 93–101 (1996).
10. Song, S., Miller, K. D. & Abbott, L. F. Competitive Hebbian learning through spike-timing-dependent synaptic plasticity. *Nat. Neurosci.* **3**, 919–926 (2000).
11. Zhang, Z., Russell, L. E., Packer, A. M., Gauld, O. M. & Häusser, M. Closed-loop all-optical manipulation of neural circuits in vivo. *Nat. Methods* **15**, 1037–1040 (2018).
12. Cassenaer, S. & Laurent, G. Hebbian STDP in mushroom bodies facilitates the synchronous flow of olfactory information in locusts. *Nature* **448**, 709–713 (2007).
13. Stopfer, M., Bhagavan, S., Smith, B. H. & Laurent, G. Impaired odour discrimination on desynchronization of odour-encoding neural assemblies. *Nature* **390**, 70–74 (1997).
14. Robbe, D. et al. Cannabinoids reveal importance of spike timing coordination in hippocampal function. *Nat. Neurosci.* **9**, 1526–1533 (2006).
15. Harris, K. D., Csicsvari, J., Hirase, H., Dragoi, G. & Buzsáki, G. Organization of cell assemblies in the hippocampus. *Nature* **424**, 552–556 (2003).
16. Wilson, M. & McNaughton, B. Dynamics of the hippocampal ensemble code for space. *Science* **261**, 1055–1058 (1993).
17. van de Ven, G. M., Trouche, S., McNamara, C. G., Allen, K. & Dupret, D. Hippocampal offline reactivation consolidates recently formed cell assembly patterns during sharp wave-ripples. *Neuron* **92**, 968–974 (2016).
18. deCharms, R. C. & Merzenich, M. M. Primary cortical representation of sounds by the coordination of action-potential timing. *Nature* **381**, 610–613 (1996).
19. Friedrich, R. W., Habermann, C. J. & Laurent, G. Multiplexing using synchrony in the zebrafish olfactory bulb. *Nat. Neurosci.* **7**, 862–871 (2004).
20. Dejean, C. et al. Prefrontal neuronal assemblies temporally control fear behaviour. *Nature* **535**, 420–424 (2016).
21. Nakazawa, K. et al. Hippocampal CA3 NMDA receptors are crucial for memory acquisition of one-time experience. *Neuron* **38**, 305–315 (2003).
22. Kelemen, E. & Fenton, A. A. Dynamic grouping of hippocampal neural activity during cognitive control of two spatial frames. *PLoS Biol.* **8**, e1000403 (2010).
23. Kubie, J. L., Levy, E. R. J. & Fenton, A. A. Is hippocampal remapping the physiological basis for context? *Hippocampus* **30**, 851–864 (2020).
24. McClelland, J. L., McNaughton, B. L. & O'Reilly, R. C. Why there are complementary learning systems in the hippocampus and neocortex: insights from the successes and failures of connectionist models of learning and memory. *Psychol. Rev.* **102**, 419–457 (1995).
25. van Dijk, M. T. & Fenton, A. A. On how the dentate gyrus contributes to memory discrimination. *Neuron* **98**, 832–845 (2018).
26. Lopes-dos-Santos, V., Ribeiro, S. & Tort, A. B. L. Detecting cell assemblies in large neuronal populations. *J. Neurosci. Methods* **220**, 149–166 (2013).
27. McKenzie, S. et al. Hippocampal representation of related and opposing memories develop within distinct, hierarchically organized neural schemas. *Neuron* **83**, 202–215 (2014).
28. Leutgeb, S. et al. Independent codes for spatial and episodic memory in hippocampal neuronal ensembles. *Science* **309**, 619–623 (2005).
29. Frank, L. M., Brown, E. N. & Wilson, M. Trajectory encoding in the hippocampus and entorhinal cortex. *Neuron* **27**, 169–178 (2000).
30. Pfeiffer, B. E. & Foster, D. J. Hippocampal place-cell sequences depict future paths to remembered goals. *Nature* **497**, 74–79 (2013).
31. Grosmark, A. D. & Buzsáki, G. Diversity in neural firing dynamics supports both rigid and learned hippocampal sequences. *Science* **351**, 1440–1443 (2016).
32. O'Neill, J., Senior, T. J., Allen, K., Huxter, J. R. & Csicsvari, J. Reactivation of experience-dependent cell assembly patterns in the hippocampus. *Nat. Neurosci.* **11**, 209–215 (2008).
33. Amaral, D. & Lavenex, P. in *The Hippocampus Book* (eds. Andersen, P., Morris, R., Amaral, D., Bliss, T. & O'Keefe, J.) Ch. 3 (Oxford University Press, 2006).
34. Middleton, S. J. & McHugh, T. J. Silencing CA3 disrupts temporal coding in the CA1 ensemble. *Nat. Neurosci.* **19**, 945–951 (2016).
35. Shipton, O. A. et al. Left–right dissociation of hippocampal memory processes in mice. *Proc. Natl Acad. Sci.* **111**, 15238–15243 (2014).
36. El-Gaby, M. et al. Archaerhodopsin selectively and reversibly silences synaptic transmission through altered pH. *Cell Rep.* **16**, 2259–2268 (2016).
37. Bragin, A. et al. Gamma (40–100 Hz) oscillation in the hippocampus of the behaving rat. *J. Neurosci.***15**, 47–60 (1995).
38. Colgin, L. L. et al. Frequency of gamma oscillations routes flow of information in the hippocampus. *Nature* **462**, 353–357 (2009).
39. Bi, G. Q. & Poo, M. M. Synaptic modifications in cultured hippocampal neurons: dependence on spike timing, synaptic strength, and postsynaptic cell type. *J. Neurosci.* **18**, 10464–10472 (1998).
40. Zenke, F. & Ganguli, S. SuperSpike: supervised learning in multilayer spiking neural networks. *Neural Comput.* **30**, 1514–1541 (2018).
41. Gütig, R. & Sompolinsky, H. The tempotron: a neuron that learns spike timing-based decisions. *Nat. Neurosci.* **9**, 420–428 (2006).
42. Kohl, M. M. et al. Hemisphere-specific optogenetic stimulation reveals left-right asymmetry of hippocampal plasticity. *Nat. Neurosci.* **14**, 1413–1415 (2011).
43. Leutgeb, J. K., Leutgeb, S., Moser, M.-B. & Moser, E. I. Pattern separation in the dentate gyrus and CA3 of the hippocampus. *Science* **315**, 961–966 (2007).

44. Jordan, J. T., Shanley, M. R. & Pytte, C. L. Behavioral state-dependent lateralization of dorsal dentate gyrus c-Fos expression in mice. *Neuronal Signal.* **3**, NS20180206 (2019).
45. Kawahara, A. et al. Neuronal major histocompatibility complex class I molecules are implicated in the generation of asymmetries in hippocampal circuitry. *J. Physiol.* **591**, 4777–4791 (2013).
46. Allegra, M., Posani, L., Gómez-Ocádiz, R. & Schmidt-Hieber, C. Differential relation between neuronal and behavioral discrimination during hippocampal memory encoding. *Neuron* **108**, 1103–1112 (2020).
47. Vertes, R. P., Hoover, W. B., Szigeti-Buck, K. & Leranth, C. Nucleus reuniens of the midline thalamus: link between the medial prefrontal cortex and the hippocampus. *Brain Res. Bull.* **71**, 601–609 (2007).
48. Stuart, G. J. & Spruston, N. Dendritic integration: 60 years of progress. *Nat. Neurosci.* **18**, 1713–1721 (2015).
49. Kastellakis, G., Cai, D. J., Mednick, S. C., Silva, A. J. & Poirazi, P. Synaptic clustering within dendrites: an emerging theory of memory formation. *Prog. Neurobiol.* **126**, 19–35 (2015).
50. Ho, J., Tumkaya, T., Aryal, S., Choi, H. & Claridge-Chang, A. Moving beyond *P* values: data analysis with estimation graphics. *Nat. Methods* **16**, 565–566 (2019).

Methods

Animals. These experiments used adult male C57BL/6J mice ($n=4$; Charles River Laboratories) and transgenic hemizygous Grik4-Cre mice[51] ($n=11$; Jackson Laboratories; C57BL/6-Tg(*Grik4-cre*)G32-4Stl/J; 006474; RRID: IMSR_JAX:006474). Animals were preselected based on their propensity to cover a novel open field and to approach a sucrose-baited dispenser within this open field. Animals were housed with their littermates up until the start of the experiment with free access to water in a dedicated housing facility with a 12-h light/12-h dark cycle (lights on at 7:00), 19–23 °C ambient temperature and 40–70% humidity. All mice were held in individually ventilated cages with wooden chew sticks and nestlets. Food was available ad libitum before the experiments (see below), and water was available ad libitum throughout. Mice were 4–7 months old at the time of testing. Experimental procedures performed on mice were in accordance with the Animals (Scientific Procedures) Act, 1986 (United Kingdom), with final ethical review by the Animals in Science Regulation Unit of the UK Home Office.

Surgical procedures. All surgical procedures were performed under deep anesthesia using isoflurane (0.5–2%) and oxygen (2 liter min^{-1}), with analgesia provided before (0.1 mg kg^{-1} Vetergesic) and after (5 mg kg^{-1} Metacam) surgery. For optogenetic manipulations, AAV5-EF1a-DIO-Arch3.0-eYFP viral vector injections (2 × 500 nl) were performed unilaterally in the dorsal CA3 on either the left or right hemispheres ($CA3^{L}$, five animals or $CA3^{R}$, six animals) of Grik4-Cre mice using stereotaxic coordinates (site 1: −1.7 mm anteroposterior, ±1.5 mm lateral and −2.1 mm ventral from bregma; site 2: −2.3 mm anteroposterior, ±2.3 mm lateral and −2.3 mm ventral from bregma). The viral vector was delivered at a rate of 100 nl min^{-1} using a glass micropipette. For electrophysiological recordings, mice were subsequently implanted 4–6 weeks later with a microdrive with 12–14 independently movable tetrodes (combined with two optic fibers for optogenetic manipulations; Doric Lenses) targeting the dorsal CA1 bilaterally[52].

Behavior. After a recovery period of at least 1 week following surgical implantation, mice were familiarized daily to the experimental paradigm, including handling, connection to the recording system and exploration of various open fields. Mice were maintained at 90–95% of their free-feeding body weight. Every day, animals explored the same (triangular) open field (the 'control enclosure'; equilateral triangle, 45-cm sides) and a new open field (45-cm outer width), wherein they were trained in the following three task phases.

Pretraining phase 1 involved conditioning mice to collect transiently available drops of 15% sucrose solution from a single liquid dispenser following a 10-s tone (Extended Data Fig. 1). Sucrose was initially available for 20 s before the drop was automatically aspirated by the dispenser. Over multiple pretraining sessions, the drop availability was gradually reduced in 5-s intervals every time the mouse successfully collected sucrose three times consecutively until a 5-s availability period was reached. To encourage full coverage across the open field and discourage behavioral persistence at the sucrose dispenser, tones were only delivered after the mouse had moved away from the dispenser to explore the open field. Pretraining phase 1 continued until mice successfully obtained reward on more than 80% of trials while uniformly exploring the open field; this typically required 5–7 d. All mice actively covered the open-field enclosure and approached the dispenser following tone presentation.

Next, for pretraining phase 2, mice experienced two pairs of wall-mounted LED displays and two identical liquid dispensers in a new spatial configuration of the learning enclosure each day (Extended Data Fig. 1). One dispenser delivered sucrose and the other delivered quinine (0.02 mM), and both drops were simultaneously available for 5 s following a 10-s tone. The identity of the dispenser delivering sucrose versus quinine solution could be inferred from the currently illuminated set of LEDs, but was not directly indicated by the LED locations (for example, Fig. 1b). The LEDs, therefore, defined a given task contingency (*X* or *Y*; Fig. 1a). On a given day of phase 2 of pretraining, mice initially explored the control enclosure for one session (~15–20 min), followed by exploration of the new learning enclosure for two sessions with only one of the two different sets of LEDs being continuously illuminated in each exploration session. Mice were allowed to rest in a sleep box before and after exploring the enclosure (~20 min per sleep/rest session). Subsequently, a total of six learning sessions (three of each contingency; ~15–25 min per session) were conducted in a pseudorandom order (for example, *X*-*Y*-*Y*-*X*-*Y*-*X*), with 15 tone presentations (thus 15 trials; intertrial interval of ~1–2 min) in each session. Sessions of the same contingency were never presented three times in a row. Sucrose and quinine were delivered simultaneously after 80% of tone presentations in each session, with the remaining 20% of tone presentations being non-reinforced (no sucrose or quinine delivered). After at least 3 d (and up to 7 d) of pretraining phase 2, animals reached an average performance of at least 80% correct choices on a given day and thus were ready for the third phase, that is the training phase.

All behavioral and electrophysiological data quantified in this study are from the training phase (Fig. 1c). Here, the procedure was identical to pretraining phase 2 except that (1) only two learning sessions of each contingency were presented in alternation (Fig. 1c; *X*-*Y*-*X*-*Y*) in a new configuration of the learning enclosure each day, and (2) a memory probe session was carried out 1 h after the final learning session of the day, with an intervening sleep session in between the last learning session and the probe. In this probe session, 24 trials were presented under extinction (that is, non-reinforced trials where neither sucrose nor quinine was delivered after the tone); 12 trials were presented in each LED-defined contingency, with pseudorandom transitions between the two sets of LEDs defining contingency *X* and *Y* while the animal was in the learning enclosure, and with the restriction that either two or five trials were delivered in succession while a given set of LEDs was active before the LEDs were switched. The first probe trials for a given recording day were equally likely to be of contingency *X* or *Y*. Probe sessions lasted 30 min in total, with trials within a given contingency occurring at a rate of one trial per min (with an additional minute delay between the last trial in one contingency and the first trial of another). Only probe sessions where animals covered at least 50% of the enclosure and completed at least four trials (that is, visited at least one dispenser for at least four trials) were included in probe analyses (48 of 71 d satisfied these criteria). Note that animals were allowed to rest/sleep in the sleep box after every session, although only three sessions were recorded: (1) pre-exploration, sleep before the first exploration session; (2) post-exploration/pre-learning, sleep after the last exploration session and (3) post-learning, sleep after the last learning session (Fig. 1c).

In addition to these two-choice discrimination training days, mice also performed 'one-contingency training days' where we tested learning and memory retrieval of a single behavioral contingency (as opposed to two behavioral contingencies as described above). Here, the task structure was identical to that of training days, but one dispenser always delivered sucrose and the other always delivered quinine regardless of the currently illuminated set of LED displays.

To quantify behavioral performance during the learning stage in each training day, we first identified for each tone trial which dispenser the animal approached within the 5-s period of reward availability. To quantify behavioral performance during the probe stage, we identified for each tone trial which dispenser the animal preferred to visit (that is, spent more time within a 5-cm vicinity of the dispenser) during the period from tone onset to 10 s after tone offset (that is, a 20-s period). For both learning and probe stages, we next classified each tone trial as being correct or incorrect depending on whether the animal had opted for the sucrose-delivering or the quinine-delivering dispenser, respectively. We finally scored behavioral performance during learning (for example, Fig. 1e) and memory performance during probe sessions (for example, Fig. 1f) by calculating the difference between the number of correct trials and the number of incorrect trials divided by the total number of completed trials. A score of 1 thus indicates that mice always visited the correct (sucrose-delivering) dispenser, while a score of −1 indicates that mice always visited the incorrect (quinine-delivering) dispenser. Note that during learning trials, because the correct dispenser in one contingency (for example, *X*) was the incorrect dispenser in the other (for example, *Y*), we display behavioral performance (for example, Fig. 1e) with respect to the current contingency, with the *y* axis ranging from 1 (correct *Y*) to 0 (chance) to 1 (correct *X*). A similar behavioral score was calculated for the exploration session (Fig. 1e) on the basis of the total number of visits to each dispenser (because there were no trials during exploration). To give equal weighting to trials in each contingency during the probe, the overall probe score for a given day was the mean of means for contingencies *X* and contingency *Y* (that is, (mean score in *Y* trials + mean score in *X* trials)/2). Data collection could not be performed blind to the conditions of the experiments because the experimenter had to be aware of which condition they had to expose each mouse to on a given day (light ON versus light OFF) and on a given session (which open-field arena/session type).

In vivo ensemble recordings and light delivery. On the morning of each recording day, optimal positioning within the CA1 pyramidal layer was performed using the local field potential (LFP) signals obtained from each tetrode[51] in search of multiunit spiking activity. Tetrodes were then left in position for ~1.5 h before commencing recordings. Tetrodes were raised at the end of each recording day to avoid possible mechanical damage overnight. Optical interrogation was performed during learning using a diode-pumped solid-state laser (Laser 2000, Ringstead) that delivers yellow light (561 nm, ~18-mW output power) to the optic fibers implanted bilaterally above the CA1 pyramidal cell layer to suppress CA3 → CA1 inputs in Arch3.0-expressing Grik4-Cre mice. Mice were accustomed to light delivery before training. During training, light was delivered for 3-min periods five times per learning session, with a 2-min light OFF gap between each light delivery. Trials occurred during the light ON epochs, and at least 1 min after the onset of each light pulse to allow sufficient time for axonal suppression[36]. Note that for the quantification of behavioral effects of input suppression, we compared light ON days to light OFF days from the same animals to provide a within-subject control.

Multichannel data acquisition. Amplification, multiplexing and digitization of signals from the electrodes were performed using a single integrated circuit located on the head of the animal (RHD2164, Intan Technologies; gain ×1,000; http://intantech.com/products_RHD2000.html). The amplified and filtered (0.09 Hz to 7.60 kHz) electrophysiological signals were digitized at 20 kHz and saved to disk along with the synchronization signals (transistor–transistor logic digital pulses) reporting the animal's position tracking, laser activation, tone presentation, sucrose and quinine drop delivery, drop removal and LED display illumination. To track

the location of the animal, three LED clusters were attached to the electrode casing and captured at 25 frames per second by an overhead color camera.

Spike detection and unit isolation. The electrophysiological signal was band-pass filtered (800 Hz to 5 kHz), and single extracellular discharges were detected through thresholding the RMS power spectrum using a 0.2-ms sliding window. Detected spikes of the individual electrodes were combined for each tetrode. To isolate spikes that putatively belonged to the same neuron, spike waveforms were first up sampled to 40 kHz and aligned to their maximal trough. Principal component analysis was applied to these waveforms ±0.5 ms from the trough to extract the first three to four principal components per channel such that each individual spike was represented by 12 waveform parameters. An automatic clustering program (KlustaKwik 2.0, https://github.com/kwikteam/klustakwik2/) was run on this principal component space, and the resulting clusters were manually recombined and further isolated based on cloud shape in the principal component space, cross-channel spike waveforms, autocorrelation and cross-correlation histograms[52]. An automated clustering was further performed using Kilosort 1.0 (ref. [53]; https://github.com/cortex-lab/KiloSort) via the SpikeForest sorting framework[54] (https://github.com/flatironinstitute/spikeforest), with units then automatically curated using metrics derived from the waveforms and spike times and verified by the operator. All sessions recorded on the same day were concatenated and clustered together. A cluster was only used for further analysis if it showed stable cross-channel spike waveforms, a clear refractory period in its autocorrelation histogram, well-defined cluster boundaries and an absence of refractory period in its cross-correlation histograms with the other clusters. This study includes a total of 1,124 CA1 principal neurons (853 on light OFF days and 271 on light ON days). Only principal neurons isolated on light OFF days were used in Figs. 2 and 3 (and Extended Data Figs. 4–7), while Fig. 4 (and Extended Data Figs. 8 and 9) included analyses on all principal neurons. All data analysis (with the exception of SWR analysis) was conducted during active locomotion periods (when the animal was running at a speed of at least 2 cm s^{-1}).

Neuronal pattern isolation and tracking. Firing patterns of coactive CA1 principal cells were detected using a statistical framework based on independent component analysis[26]. Spikes discharged by each neuron were counted in 25-ms (or 1,000-ms where indicated) time bins and standardized (*z* scored, that is, the activity of each neuron was set to have a null mean and unitary variance) to avoid an analytical bias toward neurons with higher firing rates. The neuronal population activity was represented by a matrix in which each element represents the *z*-scored spike count of a given neuron within a given time bin. We extracted coactivity patterns from this matrix in a two-step procedure. First, the number of significant coactivation patterns embedded within the neuronal population was estimated as the number of principal components of the activity matrix with variances above a threshold derived from an analytical probability function for uncorrelated data. Second, we applied an independent component analysis to extract the coactivity patterns from projection of the data into the subspace spanned by the significant principal components (that is, each coactivity pattern was captured by an independent component). Pattern detection was performed using active periods (speed > 2 cm s^{-1}) separately during the entire last session of contingency *X*, contingency *Y* (that is, X_2 and Y_2) or the exploration session of the control enclosure as appropriate. On average, we detected one coactivity pattern for every 5.5 ± 0.3 recorded neurons. To assess the enclosure or contingency specificity of coactivity patterns, we compared all patterns detected across enclosures or contingencies, respectively. This was performed as follows:

(1) We computed the cosine similarity between the weight vector representing a given pattern detected in one session (for example, X_2) and the weight vectors representing each individual pattern detected in another task session (for example, Y_2). By considering a pair of recording sessions this way, this procedure gives a matrix containing the cosine similarity values between each individual pattern detected in one session and each individual pattern detected in the other session. For each pattern, we thus identified its 'maximum similarity' value with a pattern (that is, 'the best match') of another session.

(2) Using this procedure, we obtained three distributions of maximum similarity values for the patterns detected: (i) between two sessions of the same contingency in the learning enclosure (for example, the within-contingency left matrix in Fig. 2e), (ii) between two sessions of opposing contingencies in the learning enclosure (for example, the between-contingency middle matrix in Fig. 2e) and (iii) between a given task contingency in the learning enclosure versus the patterns detected in the control enclosure (for example, the between-enclosure right matrix in Fig. 2e).

(3) We next defined contingency-discriminating patterns as patterns with between-contingency similarity values below the 90th percentile of the between-enclosure similarity distribution.

(4) To investigate the properties of such contingency-discriminating patterns, we compared them to a matched group of patterns detected in the same session but characterized with the highest between-contingency similarity values. In other words, we selected the *n* patterns with the highest between-contingency similarity scores (with *n* being the number of contingency-discriminating patterns across all recordings). We therefore isolated *n* contingency-discriminating patterns (with the lowest between-contingency similarity values) and *n* contingency-invariant patterns (with the highest within-contingency discriminating values) in each contingency. Note that the total number of contingency-discriminating patterns before exclusions is 2*n* because there are two contingencies. Subsequently, all patterns that had a within-session maximum similarity below the 90th percentile of the between-enclosure similarity distribution were excluded from further analysis.

Because detected weight vectors were typically asymmetrical (Fig. 2d), the direction where weights were highest was assigned positive weights, and principal CA1 neurons whose weights were positive and exceeded 2 s.d. from the mean were defined as pattern members (mean of 6.0 ± 0.2% member neurons for each pattern from an average of 37.1 ± 4.2 neurons recorded per day). To assess the robustness of findings regarding member neurons isolated using this membership threshold, we further used a threshold of either 1 or 3 s.d. (Extended Data Figs. 4d,e and 7d,e). In total, the analyses shown in Figs. 2 and 3 included 67 contingency-discriminating patterns (32 in contingency *X* and 35 in contingency *Y*), 152 member neurons (79 in contingency *X* and 73 in contingency *Y*) and 49 contingency-invariant patterns (104 member neurons); all patterns detected on light OFF (151 in contingency *X* and 155 in contingency *Y*) and light ON (56 in contingency *X* and 52 in contingency *Y*) days were used in Fig. 4.

The activation strength *A* of each coactivity pattern at time *t* (for example, Fig. 2d) was computed as:

$$A_t = Z_t^T P Z_t$$

Z_t is a population vector carrying the *z*-scored rate of each neuron at time *t*, *P* is the projection matrix (outer product) of the corresponding independent component and *T* is the transpose operator. A_t is therefore the squared projection of Z_t onto the component that represents the coactivity pattern. This projection represents the similarity between the independent component (representing all neurons recorded on that day) and the population rate at a given time bin of 25 ms (or 1,000 ms for patterns tracked at this window). The main diagonal of *P* was set to zero before calculating A_t to eliminate the contribution of single neurons to the coactivity pattern strength. The resulting value of A_t reflected expression strength of a particular coactivity pattern and was used in subsequent calculations of coactivity pattern emergence and spatial tuning. Therefore, the strength of a given pattern at any time point does not reflect only the small number of (member) neurons with the highest contribution to that pattern, but rather the entire weight vector representing all neurons. To determine whether pattern expression strength predicted memory probe performance, we calculated each pattern's strength during the period of tone presentation but before the animal approached either dispenser and averaged these values during theta cycles across epochs preceding correct or incorrect choices. The same calculation was performed for member neuron firing rates. Strength change across contingencies (Extended Data Fig. 8f) was calculated for each pattern as the difference between mean strength (same contingency) and mean strength (opposite contingency) normalized (divided) by mean strength (same contingency), where the 'same' contingency is the contingency in which a pattern was detected.

Significant coactivation events were defined as time points when coactivation strength was more than 2 s.d. above the mean for the learning session in which the patterns were detected. Using this threshold, the mean coactivation rate was 0.54 ± 0.02 Hz for contingency *X* and 0.52 ± 0.02 Hz for contingency *Y*. This quantification was used in Extended Data Fig. 7g,h and in example traces in Fig. 3 and Extended Data Fig. 9. For all other pattern analyses, we used the raw coactivity strength.

Spatial maps. The recording arena was divided into bins of 1.5 × 1.5 cm to generate spike count maps (the number of spikes fired in each bin) for each unit, or pattern strength map for each coactivation pattern, and an occupancy map (time spent by the animal in each bin). Rates and occupancy were calculated only during active periods (that is, speed > 2 cm s^{-1}), and bins visited less than a total of five times per session were excluded from subsequent analysis. All maps were then smoothed by convolution with a two-dimensional Gaussian kernel of a standard deviation equal to two bin widths. Finally, spatial rate maps were generated for each session individually by normalizing the smoothed spike count maps by the smoothed occupancy map. Spatial coherence reflects the similarity of the firing rate in adjacent bins and is the *z*-transform of the Pearson correlation (across all bins) between the rate in a bin and the smoothed rate of the same bin[55]. The same calculation was used on coactivity pattern strength to calculate pattern spatial coherence. The spatial correlation between maps of member neurons, or coactivation patterns, was calculated as the Pearson correlation coefficient from the direct comparison of the spatial bins between the smoothed place rate maps. This comparison was made between spatial maps of member neurons of the same patterns within the same session to assess the spatial similarity of members of the same coactivity patterns (for example, Fig. 3e) or between maps of the same member neuron across sessions to assess any possible member neuron contingency-dependent remapping (for example, Fig. 3f,g). To determine the degree to which pattern coactivations were biased by member firing fields, we calculated an infield coactivation score for each member as the spatial density of coactivations inside the member neuron's firing field (spatial bins

within 70% of the peak firing rate bin) minus the outside-the-field coactivation density divided by the sum of those two values. To match the spatial tuning of contingency-discriminating and contingency-invariant pattern members, we used the 90th percentile of the contingency-invariant pattern member spatial coherence distribution as a threshold and only included contingency-discriminating pattern members with spatial coherence values above this threshold (note that this was only done for Extended Data Fig. 7k).

Decoding. To quantify information in spike time correlations and firing rates of CA1 principal neurons, we used a Gaussian naive Bayesian classifier to decode contingency on a trial-by-trial basis (across all learning trials) from pairwise Pearson correlations of two neurons' spike trains and/or individual neuron firing rates. Uniform priors were used throughout. Because LED-defined contingencies were signaled to the animal throughout learning, we used activity across the 30-s epochs preceding tone onset, the 10-s tone and the 5-s reward availability period to ensure sufficient spikes were used for decoding. We only considered neuronal activity when the animal was at least 10 cm away from both dispensers and during active locomotion (speed > 2 cm s^{-1}). Trials with less than 10 s satisfying these criteria were excluded from analysis. Decoding was performed using either a combination of individual firing rates and 25-ms pairwise temporal correlations (for example, Fig. 2a) or pairwise correlations alone (using 25-ms bins, for example, Fig. 2b, or using 1,000-ms bins, for example, Extended Data Fig. 5j). Decoding accuracy was then compared to the mean accuracy of a null distribution generated by randomly shuffling the contingency label across trials (that is, *X* versus *Y*) 100 times. In addition, we assessed whether contingency information was present in temporal spike correlations beyond the population firing rate in two ways. First, we shuffled 25-ms correlations relative to trial labels while keeping features representing average firing rates aligned with trial labels and requantified decoding accuracy (Fig. 2a). Second, we compared decoding accuracy using only 25-ms pairwise correlations to that of using pairwise correlations between the same neurons but with spikes of each neuron shifted randomly by a value between −1,000 ms and 1,000 ms before binning. This allowed us to remove correlations due to short-timescale coincident activity while keeping coactivity associated with slower changes in population activity intact (Fig. 2b).

Explained variance. For each pair of neurons, the explained variance for task contingency was calculated using a trial-by-trial Pearson correlation on activity binned using 25-ms bins:

$$EV = \frac{SS_{\text{between contingency}}}{SS_{\text{Total}}} = \frac{nX\left(\overline{rX}-\overline{rXY}\right)^2+nY\left(\overline{rY}-\overline{rXY}\right)^2}{\sum_{i=0}^{n}\left(rX_n-\overline{rXY}\right)^{-2}+\sum_{i=0}^{n}\left(rY_n-\overline{rXY}\right)^2}$$

SS represents the sum of squares, *nX* and *nY* represent the number of trials in contingency *X* and contingency *Y*, respectively, and *rX*, *rY* and *rXY* represent temporal correlation values in *X*, *Y* and all trials respectively.

We compared this *EV* value with the mean of a null distribution generated by shuffling the contingency labels (that is, *X* versus *Y*) of trials. For decoding, we used activity across the 30-s epochs preceding tone onset, the 10-s tone and the 5-s reward availability window, only considering neuronal activity when the animal was at least 10 cm away from both dispensers and during active locomotion (speed > 2 cm s^{-1}). Trials with less than 10 s satisfying these criteria were excluded from analysis. To assess the spatial congruence of high explained variance pairs, we calculated the spatial map correlation (see Spatial maps section) of each pair in the upper fifth percentile of the *EV* distribution that was temporally positively correlated in at least one contingency. We used the maximum spatial correlation across both contingencies (for example, if neurons had more spatially correlated place fields in contingency *X* than in contingency *Y*, then the value for contingency *X* was used). We compared such spatial correlation values to those from pairs of neurons in the lower fifth percentile (low explained variance pairs) that were positively temporally correlated in both contingencies (Extended Data Fig. 7i).

Local field potential analyses. Raw LFPs were down sampled from 20 kHz to 1,250 Hz (order 8 Chebyshev type I filter was applied before decimation to avoid aliasing) and then decomposed using empirical mode decomposition (EMD[56]; https://pypi.org/project/emd/). To avoid mode mixing, we used the mask sift EMD procedure[57] with sinusoidal masks with the following frequencies: 350, 200, 70, 40, 30 and 7 Hz, which captured mid-gamma, slow-gamma and theta oscillations as isolated components. To determine individual theta cycles and theta phase, we first detected peaks and troughs of theta with absolute values higher than low-frequency component envelope (sum of all components with main frequencies below the theta signal), then a theta cycle was defined by pairs of supra-threshold troughs separated by at least 71 ms (~14 Hz) and no more than 200 ms (5 Hz) that surrounded a suprathreshold peak[58]. Theta phase was calculated by linear interpolating neighboring theta troughs, zero crossings and peaks. For nested-gamma analysis (Fig. 4c and Extended Data Fig. 8a,b,r), instantaneous envelopes and frequencies were calculated by means of the normalized Hilbert transform[59]. For the time course analysis shown in Fig. 4c and Extended Data Fig. 8r, we adopted a bootstrap procedure to keep the speed distribution of each time bin virtually equal[58]. For each experiment, we used 60-s to 30-s prelaser stimulus windows as references for speed distribution. More specifically, we calculated the histogram (linearly spaced speed bins from 2 to 30 cm s^{-1}) of instantaneous speed values for each theta cycle within that reference window; then, a bootstrap consisted of (1) subsampling theta cycles from that reference time window by randomly choosing 75% of the cycles in each speed bin (that is, maintaining the original speed histogram proportions) and (2) from all remaining time windows, for each theta cycle in the reference window, we randomly chose a cycle with matched speed (no more than 2.5% away from the reference cycle). One hundred such bootstraps were computed for each tetrode, then all tetrodes of each experiment were averaged. Figures show the mean across recording days.

SWR detection was carried out as follows. First, LFPs of each pyramidal CA1 channel were subtracted by the mean across all channels (common average reference). These re-referenced signals were then filtered for the ripple band (110 to 250 Hz; fourth order Butterworth filter), and their envelopes (instantaneous amplitudes) were computed by means of the Hilbert transform. The peaks (local maxima) of the ripple band envelope signals above a threshold (five times the median of the envelope values of that channel) were regarded as candidate events. Further, the onset and offset of each event were determined as the time points at which the ripple envelope decayed below half of the detection threshold. Candidate events passing the following criteria were determined as SWR events: (1) ripple band power in the event channel was at least two times the ripple band power in the common average reference (to eliminate common high-frequency noise), (2) an event had at least four ripple cycles (to eliminate events that were too brief) and (3) ripple band power was at least two times higher than the supraripple band defined as 200–500 Hz (to eliminate high-frequency noise not spectrally compact at the ripple band, such as spike leakage artifacts). We classified tetrodes as either being in the deep or superficial sublayer of the CA1 pyramidal cell layer based on the mean peak amplitude of the SWR events across all sleep sessions. Positive values indicated that the tetrode was in the deep sublayer (that is, closest to the stratum oriens), while negative values indicated that the tetrode was located in the superficial sublayer (that is, closest to the stratum radiatum)[60–62]. To calculate pattern member firing correlations during sleep/rest SWRs, we used SWR events as activity bins and calculated the Pearson correlations between pairs of pattern members separately across each sleep session (that is, separately for pre-exploration, pre-learning and post-learning sleep sessions; only sessions where at least 200 SWR events were detected were included in this analysis).

Anatomical and histological analysis. All mice were anesthetized with pentobarbital following completion of the experiments and transcardially perfused with PBS followed by 4% paraformaldehyde/0.1% glutaraldehyde in PBS solution. Brains were extracted and kept in 4% paraformaldehyde for at least 24 h before slicing. Coronal sections (50-µm thick) were then made and stored in PBS-azide combined with DAPI to stain neuronal somata. All sections were mounted in Vectashield (Vector Laboratories, H-1000), and images of native eYFP fluorescence and DAPI fluorescence were captured with an LSM 880 (Zeiss) confocal microscope using ZEN software (Zeiss Black 2.3).

Statistical analyses. Data were analyzed in Python 3.6 (https://www.python.org/downloads/release/python-363/) using the packages scikit-learn 0.23.2, statsmodels 0.12.1, Numpy 1.18.1, Scipy 1.4.1, Matplotlib 3.1.2, Pandas 0.25.3 and Seaborn 0.11.0. Error bars represent mean ± s.e.m. unless otherwise stated. *Ns* refer to recording days for behavioral preference figures and LFP analysis. For unit data, *Ns* refer to coactivity patterns, coactivity pattern members or all principal neurons as indicated. Where indicated, we also used mice as *Ns* for behavioral and unit data, with values averaged across days for a given mouse for behavioral data and across neurons/patterns for a given mouse for unit data. DABEST plots[50] are used throughout the manuscript to visualize effect size by plotting the data against a mean (or paired mean) difference between the left-most condition and one or more conditions on the right (right *y* axis) and comparing this difference against zero using 1,000 bootstrapped resamples. Black dots indicate the mean difference or mean paired difference (as indicated on the right *y* axis label), black ticks depict error bars representing 95% confidence intervals and shaded areas represent kernel density estimates for visualizing the resampled mean (or paired mean) difference distribution. All *P* values were calculated as specified in the figure legends. For ANOVAs, type II sums of squares were used throughout, with degrees of freedom reported in parentheses after '*F*' (for example, $F(1) = \ldots$). Data distributions were assumed to be normal for ANOVAs, but this was not formally tested. No statistical methods were used to predetermine sample sizes, but our sample sizes are similar to those reported in previous publications (for example, see refs. [25,27,31,34,63]). Neural and behavioral data analyses were conducted in an identical way regardless of the experimental condition from which the data were collected. See also the corresponding Reporting Summary.

A total of 15 mice were used in this study, where 5 animals were injected with an Archaerhodopsin-expressing construct in the left CA3 and 6 animals were injected with the same construct in the right CA3. Four mice did not receive CA3 injections.

The behavioral data in Fig. 1 (and Extended Data Figs. 2 and 3) are from light OFF training days (termed light OFF days throughout) from all 15 animals used

in this study (71 light OFF days). For behavioral quantification in Fig. 6 (and Extended Data Fig. 8), we used both light OFF and light ON days (separately as indicated) from 5 animals injected with an Archaerhodopsin-expressing construct in the left CA3 (33 light OFF days and 20 light ON days) and 6 animals injected in the right CA3 for behavioral experiments (18 light OFF days and 23 light ON days). Mice were randomly assigned to left versus right CA3-injected groups. Light OFF and light ON days were pseudorandomized and interleaved for each animal (ensuring the first day of training was always light OFF). A further 16 d of one-contingency learning were recorded (10 light OFF days and 6 light ON ($CA3^{L}$-suppression) days; Extended Data Fig. 8m).

Electrophysiological unit data in Figs. 2–5 (and Extended Data Figs. 4–7) are from light OFF days from 10 animals (23 recording days; 4 (of 5) left CA3-injected animals, 2 (of 6) right CA3-injected animals and all 4 mice without CA3 injections). Electrophysiological unit data from light ON days from 4 (of 5) left CA3-injected animals are used (8 recording days) and compared to all light OFF electrophysiological unit data in Fig. 4 (and Extended Data Figs. 8 and 9).

Reporting Summary. Further information on research design is available in the Nature Research Reporting Summary linked to this article.

Data availability

The data that support the findings of this study are available from the corresponding author upon request.

Code availability

The software used for data acquisition and analysis are available using the web links mentioned in the Methods.

References

51. Nakazawa, K. et al. Requirement for hippocampal CA3 NMDA receptors in associative memory recall. *Science* **297**, 211–218 (2002).
52. McNamara, C. G., Tejero-Cantero, Á., Trouche, S., Campo-Urriza, N. & Dupret, D. Dopaminergic neurons promote hippocampal reactivation and spatial memory persistence. *Nat. Neurosci.* **17**, 1658–1660 (2014).
53. Pachitariu, M., Steinmetz, N., Kadir, S., Carandini, M. & Harris, K. D. Kilosort: realtime spike-sorting for extracellular electrophysiology with hundreds of channels. Preprint at *bioRxiv* https://doi.org/10.1101/061481 (2016).
54. Magland, J. et al. SpikeForest, reproducible web-facing ground-truth validation of automated neural spike sorters. *eLife* **9**, e55167 (2020).
55. Zhang, S., Schönfeld, F., Wiskott, L. & Manahan-Vaughan, D. Spatial representations of place cells in darkness are supported by path integration and border information.ÿFront. *Behav. Neurosci.* **8**, 222 (2014).
56. Huang, N. E. et al. The empirical mode decomposition and the Hilbert spectrum for nonlinear and non-stationary time series analysis. *Proc. Math. Phys. Eng. Sci.* **454**, 903–995 (1998).
57. Deering, R. & Kaiser, J. F. The use of a masking signal to improve empirical mode decomposition. in *IEEE International Conference on Acoustics, Speech, and Signal Processing*. Vol. 4, 485–488 (IEEE, 2005).
58. Lopes-Dos-Santos, V. et al. Parsing hippocampal theta oscillations by nested spectral components during spatial exploration and memory-guided behavior. *Neuron* **100**, 940–952 (2018).
59. Huang, N. E. et al. On instantaneous frequency. *Adv. Adapt. Data Anal* **1**, 177–229 (2009).
60. Mizuseki, K., Diba, K., Pastalkova, E. & Buzsáki, G. Hippocampal CA1 pyramidal cells form functionally distinct sublayers. *Nat. Neurosci.* **14**, 1174–1181 (2011).
61. Oliva, A., Fernández-Ruiz, A., Buzsáki, G. & Berényi, A. Spatial coding and physiological properties of hippocampal neurons in the Cornu Ammonis subregions. *Hippocampus* **26**, 1593–1607 (2016).
62. Csicsvari, J., Hirase, H., Czurkó, A., Mamiya, A. & Buzsáki, G. Fast network oscillations in the hippocampal CA1 region of the behaving rat. *J. Neurosci.* **19**, RC20 (1999).
63. Davoudi, H. & Foster, D. J. Acute silencing of hippocampal CA3 reveals a dominant role in place field responses. *Nat. Neurosci.* **22**, 337–342 (2019).

Acknowledgements

We thank D. Bannerman and S. McHugh for helpful advice when designing the behavioral protocol, J. Westcott and B. Micklem for technical support, W. Podlaski and T. Vogels for useful discussions on neural coding models, A.J. Quinn for developing the EMD toolbox and S. Trouche, H. Barron and all the members of the Dupret laboratory for useful discussions. This work was supported by the Biotechnology and Biological Sciences Research Council UK (BB/N00597X/1 to D.D. and BB/N006836/1 to O.P.) and the Medical Research Council UK (MC_UU_12024/3 and MC_UU_00003/4 to D.D.).

Author contributions

M.E., O.P. and D.D. conceptualized the study; M.E. and D.D. designed the experiments; M.E., H.M.R., P.V.P., N.C.-U., L.A.M.S. and I.P.L. performed the experiments and acquired the data; M.E., V.L. and A.M. preprocessed the data; M.E. and V.L. analyzed the data; M.E. and D.D. wrote the manuscript and D.D. supervised the project. All authors discussed the results and commented on the manuscript.

Competing interests

The authors declare no competing interests.

Additional information

Extended data is available for this paper at https://doi.org/10.1038/s41593-021-00820-w.

Supplementary information The online version contains supplementary material available at https://doi.org/10.1038/s41593-021-00820-w.

Correspondence and requests for materials should be addressed to M.E.-G. or D.D.

Peer review information *Nature Neuroscience* thanks Rosa Cossart, Steven Siegelbaum, and the other, anonymous, reviewer(s) for their contribution to the peer review of this work.

Reprints and permissions information is available at www.nature.com/reprints.

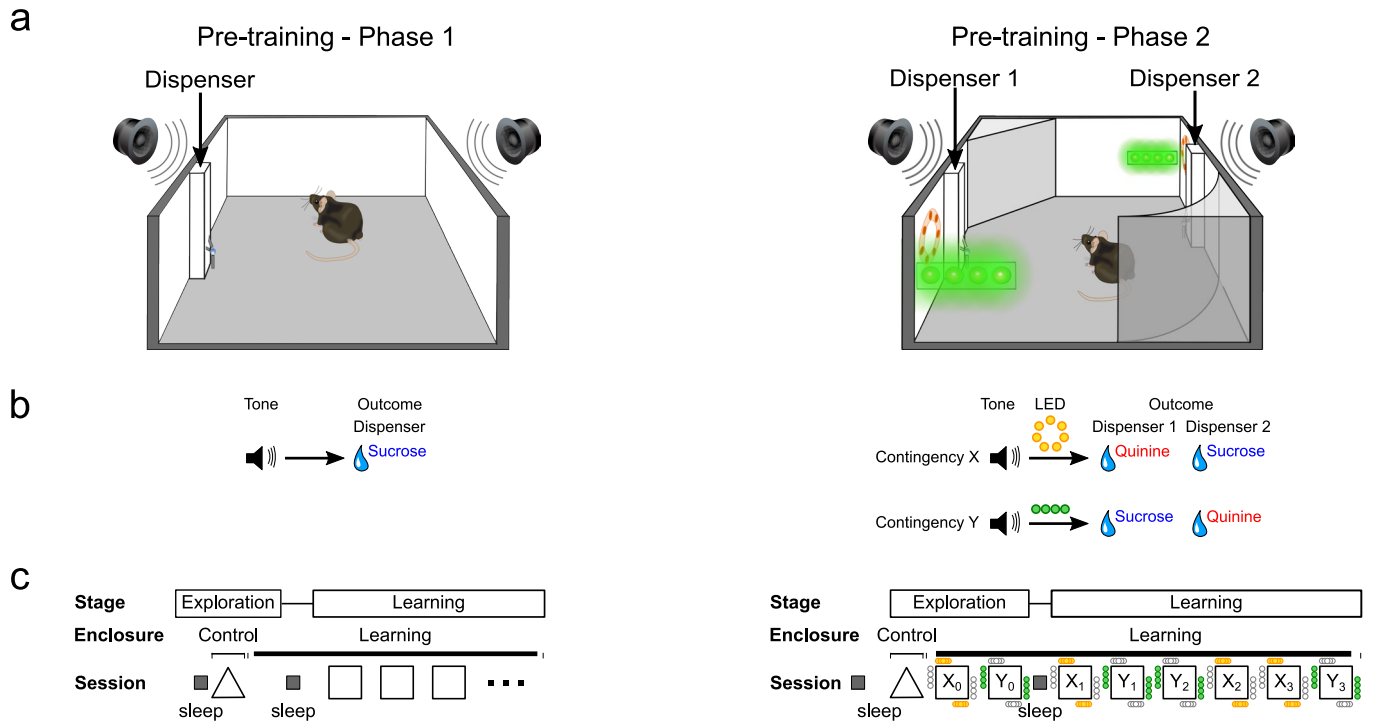

Extended Data Fig. 1 | Schematics of pretraining protocol. Schematics of pretraining phases 1 (left) and 2 (right). **a**, Schematic of example learning enclosures. **b**, Learning in pretraining phase 1 involved associating a tone with delivery of sucrose from one dispenser. In pretraining phase 2, animals learned two new LED-tone-outcome associations each day. **c**, In pretraining phase 1 animals initially explored the control enclosure and then experienced between 2-6 sessions of tone-defined trials. In pretraining phase 2, after exploring the control enclosure and the learning enclosure (with each LED set active in turn), tone-defined trials were presented in 6 learning sessions (3 in contingency X and 3 in contingency Y) that were pseudo-randomly ordered each day. No probe tests were carried out in either pretraining phase.

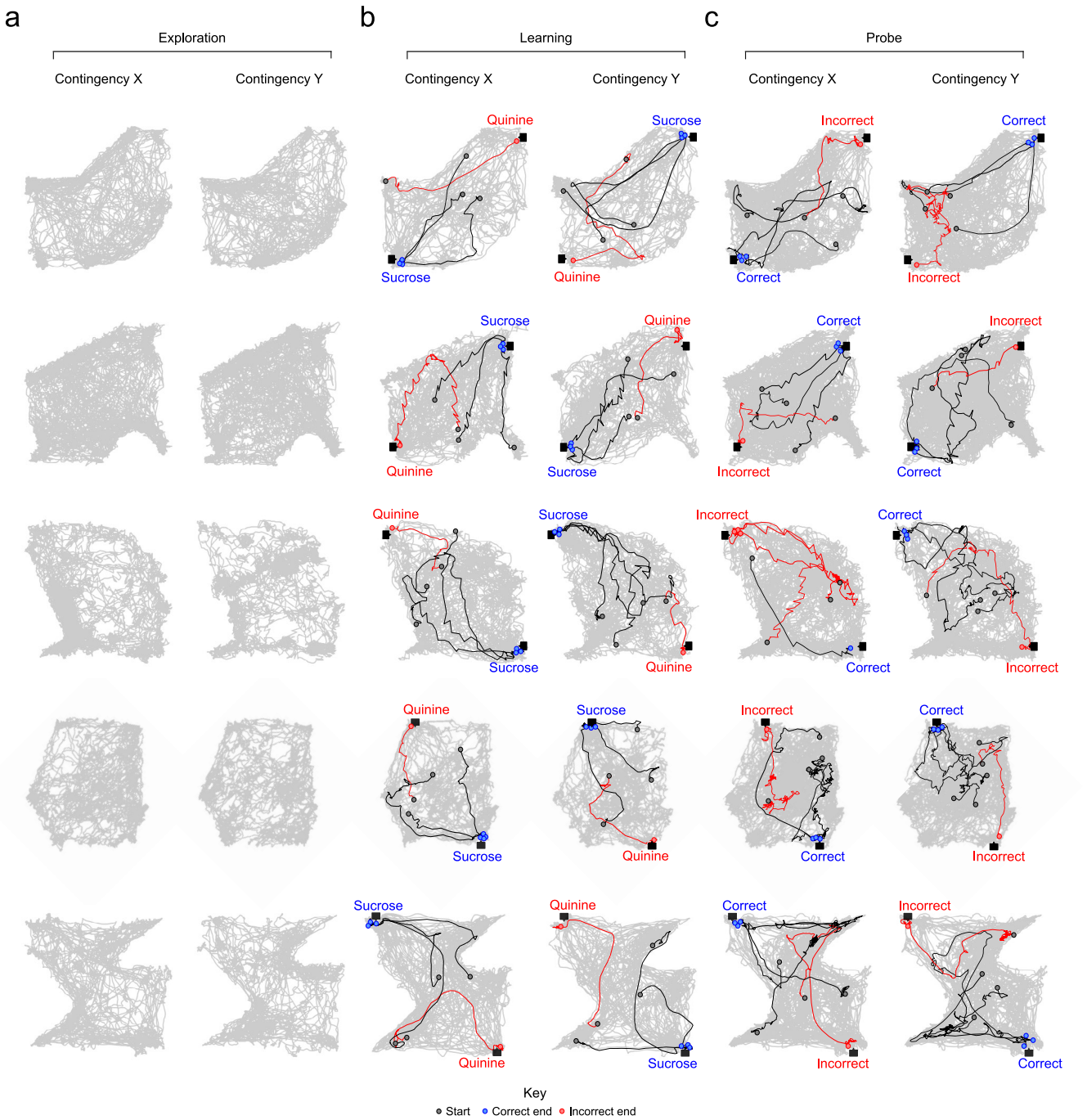

Extended Data Fig. 2 | Examples of enclosure set ups and animal paths across task stages and recording days. Enclosure set ups across distinct behavioral days. Animal coverage represented in grey. **a**, Example coverage paths for pre-learning exploration of learning enclosures. **b**, Example animal paths during learning trials in contingency *X* and contingency *Y*. **c**, Example animal paths during probe trials in contingency *X* and contingency *Y*. Paths of the animal during trials (correct path: black; incorrect path: red) are overlaid onto overall coverage (grey) for a single learning session. Black circles represent path starting points; blue and red circles represent correct and incorrect end points, respectively.

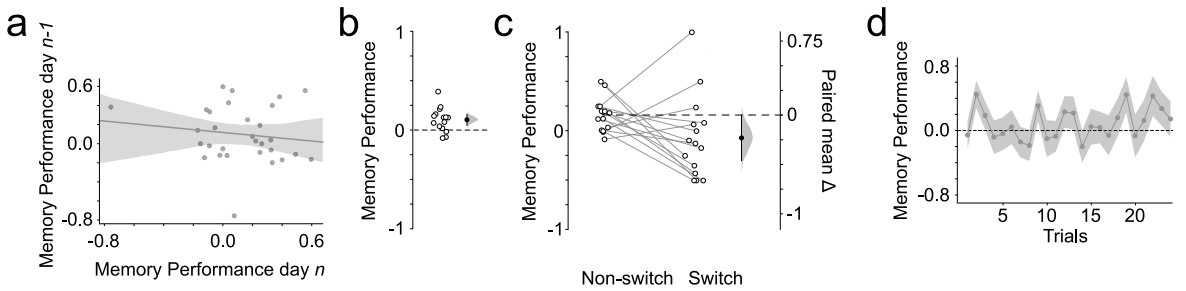

Extended Data Fig. 3 | Dynamics of memory performance. a, Lack of a relationship between performance on probe trials of a recording day and those of the previous day (Regression line shown in dark grey; light grey shaded area represents 95% confidence intervals). Linear regression of probe performance on day n against probe performance on day 'n-1': r = -0.155, P = 0.413. **b**, Behavioral performance during memory probe test, per mouse. Here the memory performance for each individual mouse is averaged across days, with each data point showing average performance for a single mouse (mean performance=0.10 ± 0.03). **c**, Probe performance (per mouse) is weaker during the first trial following a switch in LED displays (switch trials; Mean performance: -0.07 ± 0.11) compared to subsequent trials (non-switch trials; Mean performance: 0.16 ± 0.04). **d**, Probe performance does not change systematically across probe trials and hence no further learning is observed during memory retrieval. Linear regression of performance against trial number r = 0.030, P = 0.442.

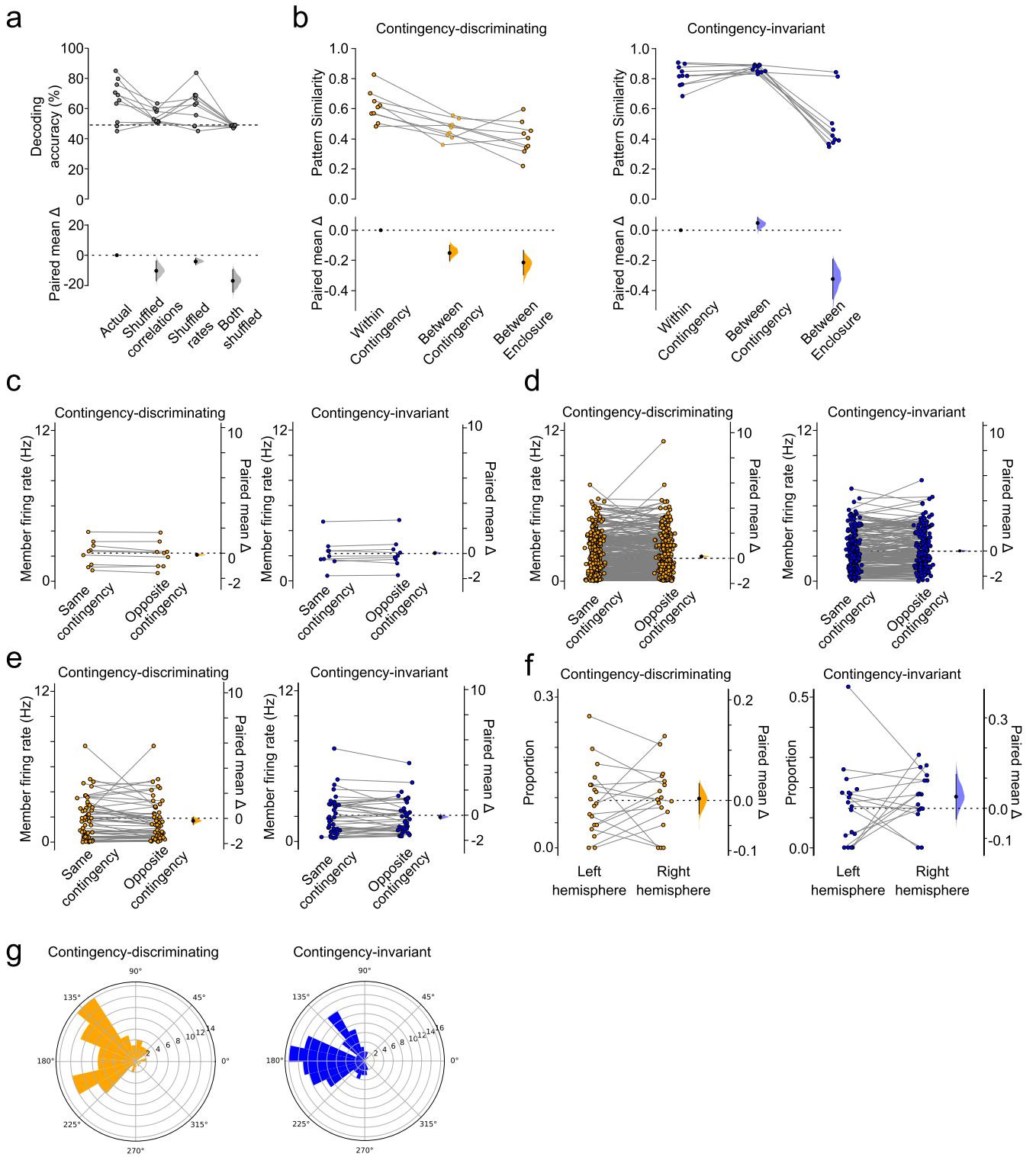

Extended Data Fig. 4 | See next page for caption.

Extended Data Fig. 4 | Within- and between-contingency properties of coactivity patterns and their member neurons. a, A Gaussian Naive Bayesian classifier was trained to decode contingencies using a combination of CA1 principal neuron firing rates and pairwise correlations. Shuffling rates, correlations or both impairs classifier performance. Data points represent individual mice. Mean accuracy; actual: 65.3 ± 4.3%, shuffled correlations: 55.0 ± 1.5%, shuffled rates: 61.2 ± 3.7%, both shuffled: 48.3 ± 0.2%; N = 10 mice. **b**, Cosine similarity of contingency-discriminating and contingency-invariant patterns across conditions per mouse. Contingency-discriminating: Within-contingency: 0.62 ± 0.03, between-contingency: 0.47 ± 0.02, between-enclosure: 0.41 ± 0.04; Contingency-invariant: Within-contingency: 0.82 ± 0.02, between-contingency: 0.87 ± 0.01, between-enclosure: 0.49 ± 0.06. Note that N = 10 animals for contingency-invariant patterns but 9 animals for contingency-discriminating patterns as no such patterns could be detected in one animal. **c**, Average firing rate of contingency-discriminating and contingency-invariant member neurons per mouse. Contingency-discriminating: Same contingency: 2.22 ± 0.33 Hz, opposite contingency: 2.09 ± 0.33 Hz; Contingency-invariant: Same contingency: 2.15 ± 0.41 Hz, opposite contingency: 2.20 ± 0.42 Hz. N = 9 animals for contingency discriminating and contingency invariant patterns as for one animal, none of the detected contingency-invariant patterns had 'members' (that is neurons with a weight of more than 2 standard deviations above the pattern weight vector mean). Average firing rate of contingency-discriminating and contingency-invariant member neurons using (**d**) 1 standard deviation (Contingency-discriminating: Same contingency: 2.00 ± 0.09 Hz, opposite contingency: 1.95 ± 0.09 Hz; Contingency-invariant: Same contingency: 2.38 ± 0.11 Hz, opposite contingency: 2.42 ± 0.11 Hz) or (**e**) 3 standard deviations as weight thresholds for defining pattern members (Contingency-discriminating: Same contingency: 1.93 ± 0.23 Hz, opposite contingency: 1.70 ± 0.22 Hz; Contingency-invariant: Same contingency: 2.06 ± 0.25 Hz, opposite contingency: 1.93 ± 0.21 Hz). **f**, Proportion of principal neurons recorded from the CA1 on the left or the right hemisphere that are members of contingency-discriminating patterns (Mean proportion: left hemisphere: 0.104 ± 0.017, right hemisphere: 0.087 ± 0.015) or contingency-invariant patterns (Mean proportion: left hemisphere: 0.129 ± 0.022, right hemisphere: 0.179 ± 0.033). **g**, Contingency discriminating pattern members showed a trend towards a preference for earlier phases of theta cycles compared to contingency invariant pattern members (Mean theta-phase preference, with respect to theta peak; contingency-discriminating pattern members: 156 ± 6°; contingency-invariant pattern members: 174 ± 5°; Watson-Wheeler test: W(2)=5.23, P = 0.073).

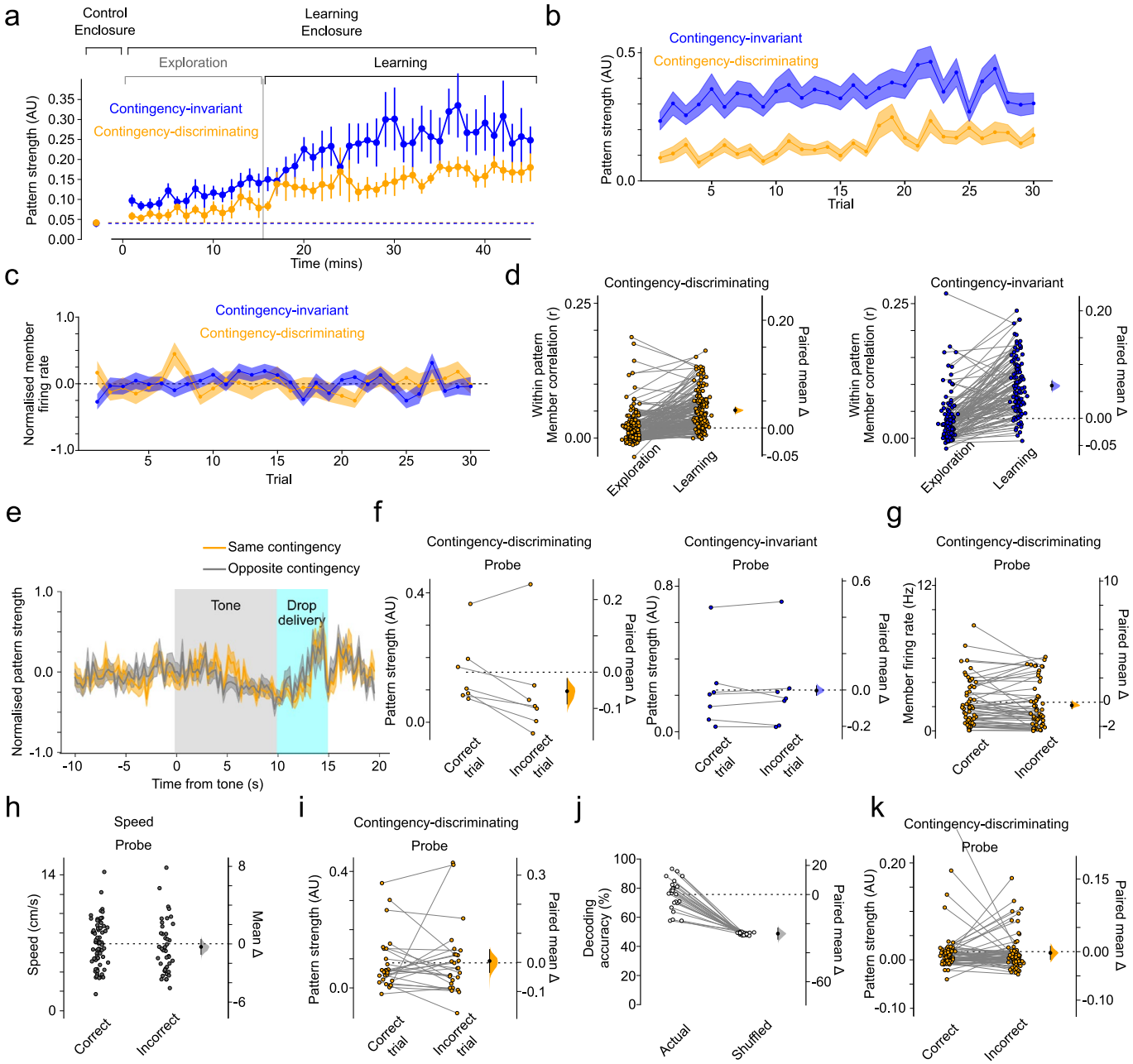

Extended Data Fig. 5 | See next page for caption.

Extended Data Fig. 5 | Contingency discriminating and invariant coactivity patterns show distinct relationships to task phase and performance. **a**, Time-course of pattern strength changes with mice as Ns. Contingency X-discriminating and contingency Y-discriminating patterns were pooled and the strength of all patterns of a given type in its preferred contingency were averaged per mouse and the mean value quantified in exploration/learning sessions. Dashed lines represent mean pattern strength in Control enclosure. Linear regression of strength against time during Exploration (contingency-invariant: $r = 0.27$, $P = 8.15\times10^{-4}$; contingency-discriminating: $r = 0.20$, $P = 0.02$) and Learning (contingency-invariant: $r = 0.19$, $P = 9.30\times10^{-4}$; contingency-discriminating: $r = 0.21$, $P = 4.92\times10^{-4}$). Slopes of contingency invariant patterns showed a trend towards being higher than those of contingency discriminating patterns during exploration (slope = 0.0041 ± 0.0012 and 0.0025 ± 0.0015 units/minute respectively; Mann Whitney U test (two-sided): $U = 25.0$, $P = 0.06$) but not during learning (slope = 0.0038 ± 0.0015 and 0.0021 ± 0.0007 units/minute respectively; Mann Whitney U test (two-sided): $U = 36.0$, $P = 0.24$). N = 10 animals for contingency invariant patterns but 9 animals for contingency discriminating patterns as no such patterns were detected in one animal. **b**, Increases in contingency-invariant and contingency-discriminating pattern strengths plotted as a function of learning trials. Contingency X-discriminating and Y-discriminating patterns were pooled, and the coactivity strength of each pattern was quantified in learning trials of its preferred contingency. Linear regression of strength against trials (contingency-invariant: $r = 0.04$, $P = 0.020$; contingency-discriminating: $r = 0.13$, $P = 1.05\times10^{-8}$). Shaded area represents variability (Standard error of the mean) across coactivity patterns. **c**, No changes in member neuron firing rates (z-scored) across learning trials. Linear regression of firing rate against trials (contingency-invariant: $r = 0.0016$, $P = 0.94$; contingency-discriminating: $r = 0.0022$, $P = 0.94$). Shaded area represents variability (Standard error of the mean) across coactivity pattern members. **d**, Temporal correlations (Pearson r values) amongst each member neuron of a pattern and other members in the same pattern between exploration and learning (Mean Pearson correlation: Contingency-invariant members: exploration: 0.037 ± 0.004, learning: 0.098 ± 0.005; contingency-discriminating members: exploration: 0.019 ± 0.003, learning: 0.052 ± 0.003). **e**, Z-scored contingency discriminating pattern strength in the same contingency and the opposite contingency during tone and drop delivery. This is the point when animals' behavior is maximally different between contingencies, as animals head towards opposite dispensers (Fig. 1e and Extended Data Fig. 2b). Despite this, the normalized time course of coactivity pattern strength was indistinguishable across contingencies (Two way repeated measures ANOVA: No main effect of contingency: $F(1)=1.5\times10^{-26}$, $P = 1.00$, $\eta^2 = 9.39\times10^{-31}$, Main effect of time: $F(117)=3.41$, $P = 7.61\times10^{-32}$, $\eta^2 = 0.025$, No contingency:time interaction: $F(117)=0.76$, $P = 0.98$, $\eta^2 = 0.006$). **f**, Pattern strength before the animal's choice during probe trials, on days where overall probe performance was above chance, averaged per mouse. Contingency discriminating mean strength: correct: 0.14 ± 0.04, incorrect: 0.09 ± 0.05; contingency-invariant: correct: 0.23 ± 0.08, incorrect: 0.23 ± 0.09. N = 7 animals for both contingency-discriminating and contingency-invariant patterns reflecting the number of animals with recording days in which: 1) units were recorded and isolated; 2) animals performed above chance in the probe; 3) coactivity patterns of the indicated type were detected. **g**, Contingency-discriminating pattern member firing rate is indistinguishable before correct vs incorrect probe trials on days where overall probe performance was above chance. Mean member rate: correct: 2.32 ± 0.26 Hz, incorrect: 2.15 ± 0.26 Hz. **h**, Mouse running speed before correct and incorrect trials. Mean speed: correct: 6.90 ± 0.28 $cm.s^{-1}$, incorrect: 6.58 ± 0.43 $cm.s^{-1}$. **i**, Contingency-discriminating coactivity patterns are indistinguishable before correct trials compared to incorrect trials on days when the animal's overall probe performance is not above chance level. Mean strength: correct: 0.086 ± 0.019, incorrect: 0.090 ± 0.023. **j**, Decoding accuracy using 1000 ms pairwise correlations compared to shuffled controls. (Mean accuracy; Actual: 75.7 ± 2.1%, shuffled: 48.8 ± 0.2%; N = 23 recording days). **k**, Contingency-discriminating coactivity patterns, detected across 1000 ms windows, are not stronger before correct compared to incorrect choices on memory probe trials, on days where overall probe performance was above chance. Mean strength: correct: 0.017 ± 0.006, incorrect: 0.016 ± 0.004.

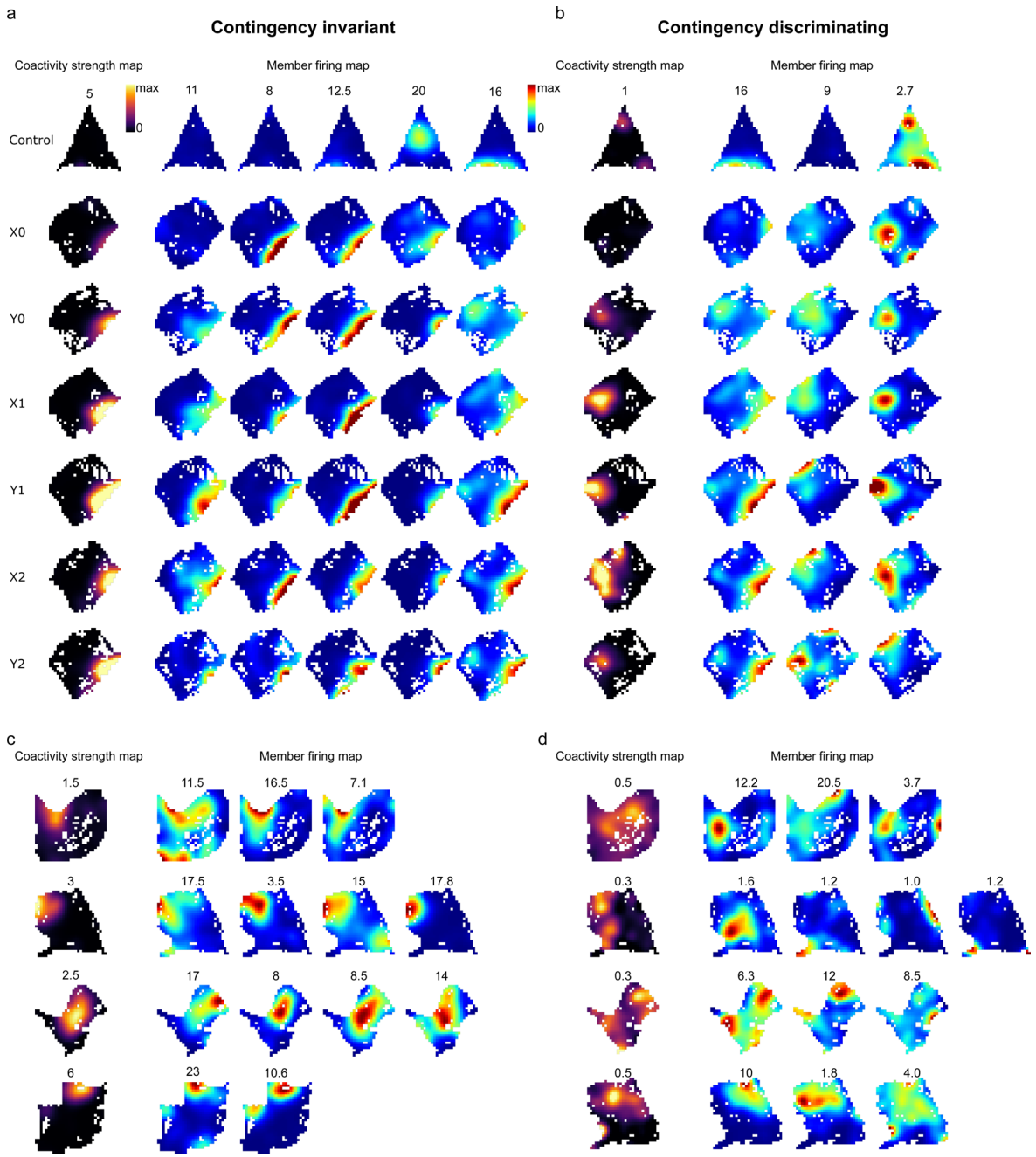

Extended Data Fig. 6 | Example pattern activation and member firing rate maps. Example pattern activation maps and corresponding place maps of pattern member neurons for (**a**) a contingency-invariant and a concomitantly recorded (**b**) contingency-discriminating coactivity pattern across all sessions. Note that the right most member of the contingency-invariant pattern is also a member of the contingency-discriminating pattern. Further examples of coactivity pattern and strength maps and member rate maps for (**c**) contingency invariant and (**d**) contingency discriminating patterns. Maps are shown for the session in which these patterns were detected. Maximum firing rate (in Hz) or maximum coactivity strength (AU) are shown above each firing rate map or pattern strength map, respectively.

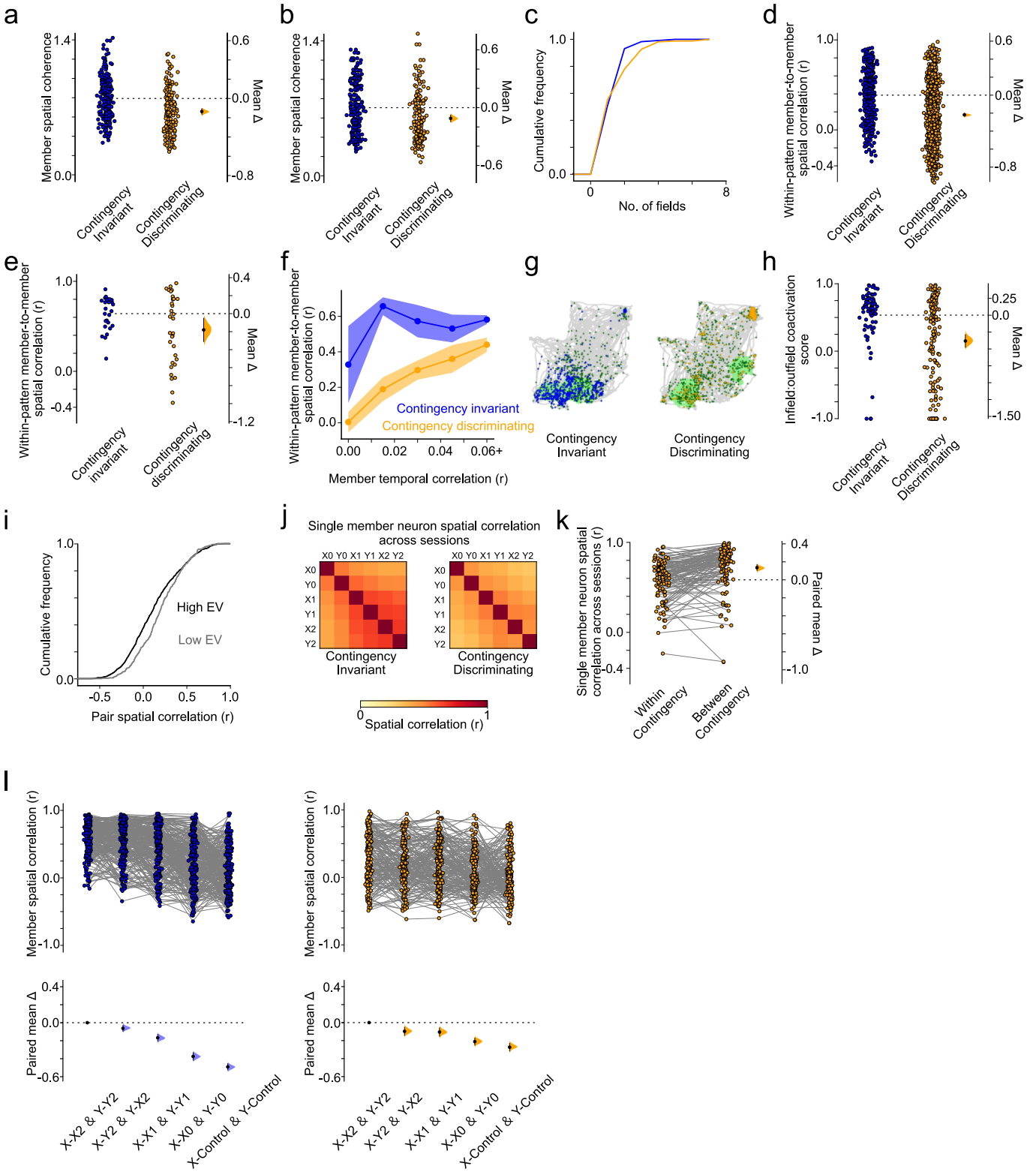

Extended Data Fig. 7 | See next page for caption.

Extended Data Fig. 7 | Spatial firing properties of coactivity pattern members. Spatial coherence of contingency-invariant pattern members is higher than that of contingency-discriminating pattern members (**a**) in the learning (Mean spatial coherence: contingency-invariant: 0.79 ± 0.01, contingency-discriminating: 0.66 ± 0.02) and (**b**) in the control enclosures (Mean spatial coherence: contingency-invariant: 0.71 ± 0.02, contingency-discriminating: 0.60 ± 0.02). **c**, Cumulative distribution of spatial firing field numbers for contingency-discriminating and contingency-invariant pattern members. (Mean field number: contingency-invariant: 1.59 ± 0.07, contingency-discriminating: 1.79 ± 0.09; Kolmogorov-Smirnov test (two-sided): D = 0.15, P = 0.08. Member neuron firing fields are less spatially overlapping for contingency-discriminating than contingency-invariant patterns using (**d**) 1 standard deviation (Mean spatial correlation: contingency-invariant: 0.39 ± 0.01, contingency-discriminating: 0.17 ± 0.01) or (**e**) 3 standard deviations (Mean spatial correlation: contingency-invariant: 0.64 ± 0.04, contingency-discriminating: 0.46 ± 0.07) as weight thresholds for defining pattern members. **f**, Pairwise spatial correlations of contingency-discriminating pattern members are lower than those of contingency-invariant pattern members regardless of the degree of temporal correlation between the member neurons. Two-way ANOVA: main effect of pattern type ($F(1)=27.0$, $P = 3.87\times10^{-7}$, $\eta^2 = 0.073$) and temporal correlation ($F(4)=9.3$, $P = 4.12\times10^{-7}$, $\eta^2 = 0.102$). No pattern type: temporal correlation interaction ($F(4)=1.7$, $P = 0.14$, $\eta^2 = 0.019$). **g**, Example coverage traces (gray) with overlaid spiking activity (dots) of a member of a contingency-invariant (left) and a member of a contingency-discriminating (right) coactivity pattern. Spikes during a co-activation event of a given pattern are marked in blue (contingency-invariant) or orange (contingency-discriminating), while the remaining spikes are marked in dark green. Spatial firing field of the member neuron is indicated by light green shading. **h**, Infield versus outfield co-activation score for member neurons of contingency-invariant and contingency-discriminating patterns (Mean score: contingency-invariant: 0.56 ± 0.04, contingency-discriminating: 0.18 ± 0.05). **i**, Pairwise spatial correlations of high explained variance and low explained variance principal cell pairs. Mean spatial correlation: High explained variance pairs (N = 993): 0.134 ± 0.010, low explained variance pairs (N = 369): 0.204 ± 0.014; Mann Whitney U test (two-sided): $U = 155648.0$, $P = 9.69\times10^{-6}$. **j**, Matrices showing mean spatial correlations of members of contingency invariant (left) and contingency-discriminating (right) patterns across all sessions. **k**, Spatial correlation of each contingency discriminating pattern member neuron across sessions of the same contingency or of opposite contingencies showing only member neurons with spatial coherence matching that of contingency-invariant pattern members (Mean spatial correlation: within-contingency 0.58 ± 0.02, between-contingency: 0.72 ± 0.02). **l**, Spatial correlations between members of the same contingency-invariant (left) or contingency-discriminating (right) patterns across sessions. For both pattern types spatial correlations amongst pairs of neurons of the same coactivity patterns were higher during the learning stage than during the exploration stage further reflecting the development of these patterns with learning. Spatial correlations amongst members of the same contingency discriminating or those of contingency-invariant patterns were lowest in the control enclosure and highest in the last learning sessions, confirming the enclosure-selectivity of hippocampal maps. Key to x-axis labels: first letter denotes contingency in which pattern was detected, subsequent letters denote session in which spatial maps of members were computed (for example X-Y2 are the spatial maps of members of coactivity patterns detected in contingency X, plotted in session Y2; that is second learning session of contingency Y). Mean spatial correlation: contingency-invariant: X-X2 & Y-Y2 (pooled): 0.605 ± 0.015, X-Y2 & Y-X2: 0.543 ± 0.018, X-X1 & Y-Y1: 0.438 ± 0.021, X-X0 & Y-Y0: 0.230 ± 0.023, X-Control & Y-Control: 0.114 ± 0.021; contingency-discriminating: X-X2 & Y-Y2: 0.297 ± 0.027, X-Y2 & Y-X2: 0.200 ± 0.025, X-X1 & Y-Y1: 0.191 ± 0.026, X-X0 & Y-Y0: 0.086 ± 0.023, X-Control & Y-Control: 0.023 ± 0.024.

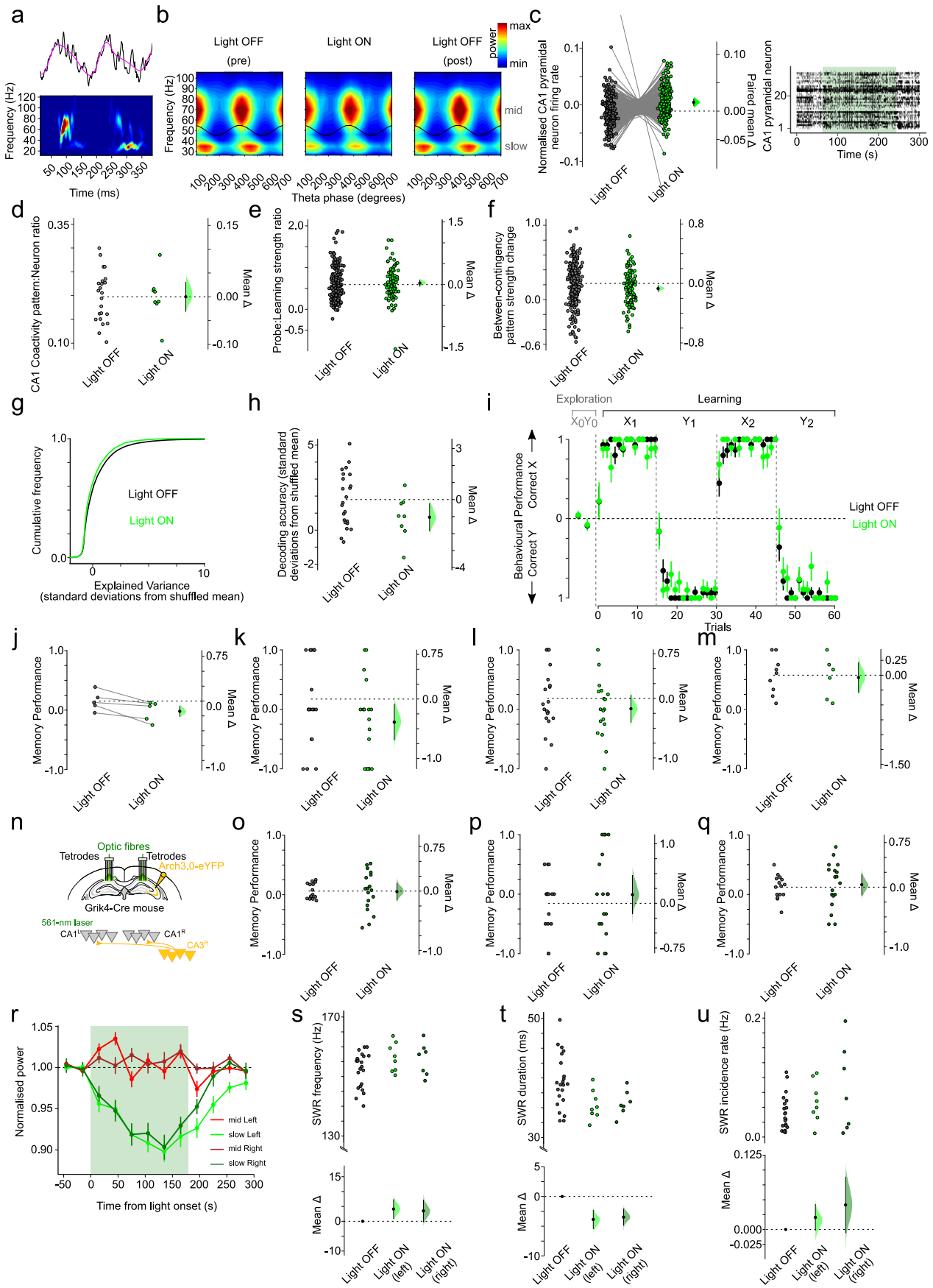

Extended Data Fig. 8 | See next page for caption.

Extended Data Fig. 8 | Behavioral and neural effects of silencing left or right hemisphere originating CA3-CA1 inputs. a, Example LFP trace containing theta-nested mid and slow gamma oscillations (top; raw trace and theta component as black and magenta traces, respectively) along with its time-frequency representation (bottom) (**b**) Example of the selective effect of $CA3^{L} \rightarrow$ CA1 input suppression on the slow but not the mid gamma oscillations. Shown are Hilbert-spectra as a function of ongoing theta phase for pre, during and post light delivery in a representative session (colors represent the same scale in all three panels). Theta cycles were subsampled to maintain instantaneous speed distributions across panels. **c**, Firing rate of CA1 principal neurons is increased by light delivery (Mean normalized (z-scored) firing rate: light OFF epochs: -0.011 ± 0.002, light ON epochs (1 minute after light onset): 0.004 ± 0.002; *right*, example raster plot during light ON period for one light ON epoch in a single recording day). **d**, The ratio of detected coactivity patterns to CA1 principal neurons is unaltered by $CA3^{L} \rightarrow$ CA1 input suppression (Mean pattern-to-neuron ratio: Light OFF days: 0.20 ± 0.01, Light ON days: 0.20 ± 0.02). **e**, Reinstatement strength of all coactivity patterns is unaltered by $CA3^{L} \rightarrow$ CA1 input suppression (Mean probe:learning pattern strength ratio: Light OFF: 0.59 ± 0.02, Light ON: 0.63 ± 0.04). Results in panels e and d show that input suppression does not alter the overall organisation of CA1 neurons into coactivity patterns nor the cross-session stability of such coactivity. **f**, The strength of coactivity patterns detected in the CA1 under $CA3^{L} \rightarrow$ CA1 input suppression is less sensitive to contingencies compared to light OFF days (Mean pattern strength change across contingencies: Light OFF days: 0.22 ± 0.01, Light ON days: 0.15 ± 0.02). **g**, Explained variance for contingency is higher in light OFF days compared to days with $CA3^{L} \rightarrow$ CA1 input suppression. Mean normalised explained variance (standard deviations from mean): Light OFF days: 0.36 ± 0.01 (N = 19852 neuron pairs), Light ON days (N = 5696 neuron pairs): 0.10 ± 0.02; Mann Whitney U test (two-sided): $U = 51962023.0$, $P = 9.36 \times 10^{-21}$. **h**, $CA3^{L} \rightarrow$ CA1 input suppression impairs Gaussian naïve Bayesian decoding accuracy using short-timescale (25 ms) correlations (Mean normalised decoding accuracy (standard deviations from mean): Light OFF days (N = 23 days): 1.80 ± 0.33, Light ON days (N = 8 days): 0.75 ± 0.45). **i**, $CA3^{L} \rightarrow$ CA1 input suppression does not impair performance during learning trials. Mean performance: Light OFF: 0.90 ± 0.02 (n = 31 days), Light ON: 0.86 ± 0.02 (n = 20 days); Mann Whitney U test (two-sided): $U = 240.0$, $P = 0.09$. **j**, Comparison of mean probe performance on light OFF and light ON ($CA3^{L} \rightarrow$ CA1 input suppression) days averaged per animal. (Mean performance: Light OFF days: 0.15 ± 0.07, Light ON days: -0.02 ± 0.08). Effect of $CA3^{L} \rightarrow$ CA1 input suppression on performance on (**k**) the first trial following a switch in LED displays ('switch' trials; Mean performance: Light OFF days: 0.18 ± 0.17, Light ON days: -0.21 ± 0.16) and on (**l**) subsequent trials ('non-switch' trials: Light OFF days: 0.18 ± 0.12, Light ON days: 0.01 ± 0.11). **m**, Suppressing $CA3^{L}$ inputs to CA1 during learning does not impair memory performance in probe trials when each LED set signals the same contingency (same dispenser-sucrose and dispenser-quinine pairing) throughout all learning sessions ('One-contingency training days'; Mean performance: Light OFF days: 0.57 ± 0.11, Light ON days: 0.54 ± 0.14). **n**, Schematic of $CA3^{R} \rightarrow$ CA1 optogenetic suppression protocol. $CA3^{R}$ neurons were transduced with Archaerhodopsin 3.0 in Grik4-Cre mice (n = 6) and their axonal projections in the CA1 targeted bilaterally during learning trials with yellow 561nm-light delivery from implanted optic fibres. $CA3^{R} \rightarrow$ CA1 input suppression during learning of the two-contingency task does not impair performance in probe trials, when taking (**o**) all (Mean performance: Light OFF: 0.06 ± 0.03, Light ON: 0.05 ± 0.08), (**p**) switch (Mean performance: Light OFF: -0.16 ± 0.12, Light ON: -0.01 ± 0.17) or (**q**) non-switch trials (Mean performance: Light OFF: 0.12 ± 0.05, Light ON: 0.17 ± 0.09). **r**, Suppression of $CA3^{R} \rightarrow$ CA1 input reduces the power of theta-nested slow gamma oscillations to a similar extent as with $CA3^{L} \rightarrow$ CA1 input suppression without affecting mid gamma oscillations. Two-way repeated measures ANOVA: Slow gamma: Main effect of light ($F(1) = 64.2$, $P > 0.001$, $\eta^2 = 0.592$), no main effect of CA3 hemisphere ($F(1) = 0.571$, $P = 0.457$, $\eta^2 = 0.005$) on normalised gamma power; Mid gamma: No main effect of light ($F(1) = 1.22$, $P = 0.281$, $\eta^2 = 0.029$), no main effect of CA3 hemisphere ($F = 0.226$, $P = 0.639$, $\eta^2 = 0.005$) on normalised gamma power. **s**, SWR frequency increases with suppression of either $CA3^{L} \rightarrow$ CA1 or $CA3^{R} \rightarrow$ CA1 inputs (mean frequency: Light OFF days: 152 ± 1 Hz, Light ON days (left): 156 ± 2 Hz, Light ON days (right): 155 ± 2 Hz. **t**, Awake sharp-wave ripple (SWR) duration is reduced by suppression of either $CA3^{L} \rightarrow$ CA1 or $CA3^{R} \rightarrow$ CA1 inputs (mean duration: Light OFF days: 39 ± 1 ms, Light ON days (left): 35 ± 1 ms, Light ON days (right): 36 ± 1 ms). This reduction is therefore not sufficient to explain the selective impairment of memory performance after suppressing $CA3^{L} \rightarrow$ CA1 but not $CA3^{R} \rightarrow$ CA1 inputs. **u**, Incidence rates of awake SWRs during suppression of either $CA3^{L} \rightarrow$ CA1 or $CA3^{R} \rightarrow$ CA1 inputs (mean incidence rate: Light OFF days: 0.039 ± 0.006 Hz, Light ON (left) days: 0.059 ± 0.012 Hz, Light ON (right) days: 0.080 ± 0.027 Hz). We did not observe a reduction in awake SWR incidence rates, unlike a previous study using bilateral silencing of CA3 neurons in rats[63]. Possible co-occurrence of SWR generating processes in the CA3 across hemispheres may explain why unilateral silencing does not impair the incidence rate of CA1 SWRs. Nevertheless, the reduction in SWR duration seen when silencing unilateral CA3 inputs from either hemisphere suggests that input from the CA3 on both hemispheres is needed for the full expression of a given CA1 SWR.

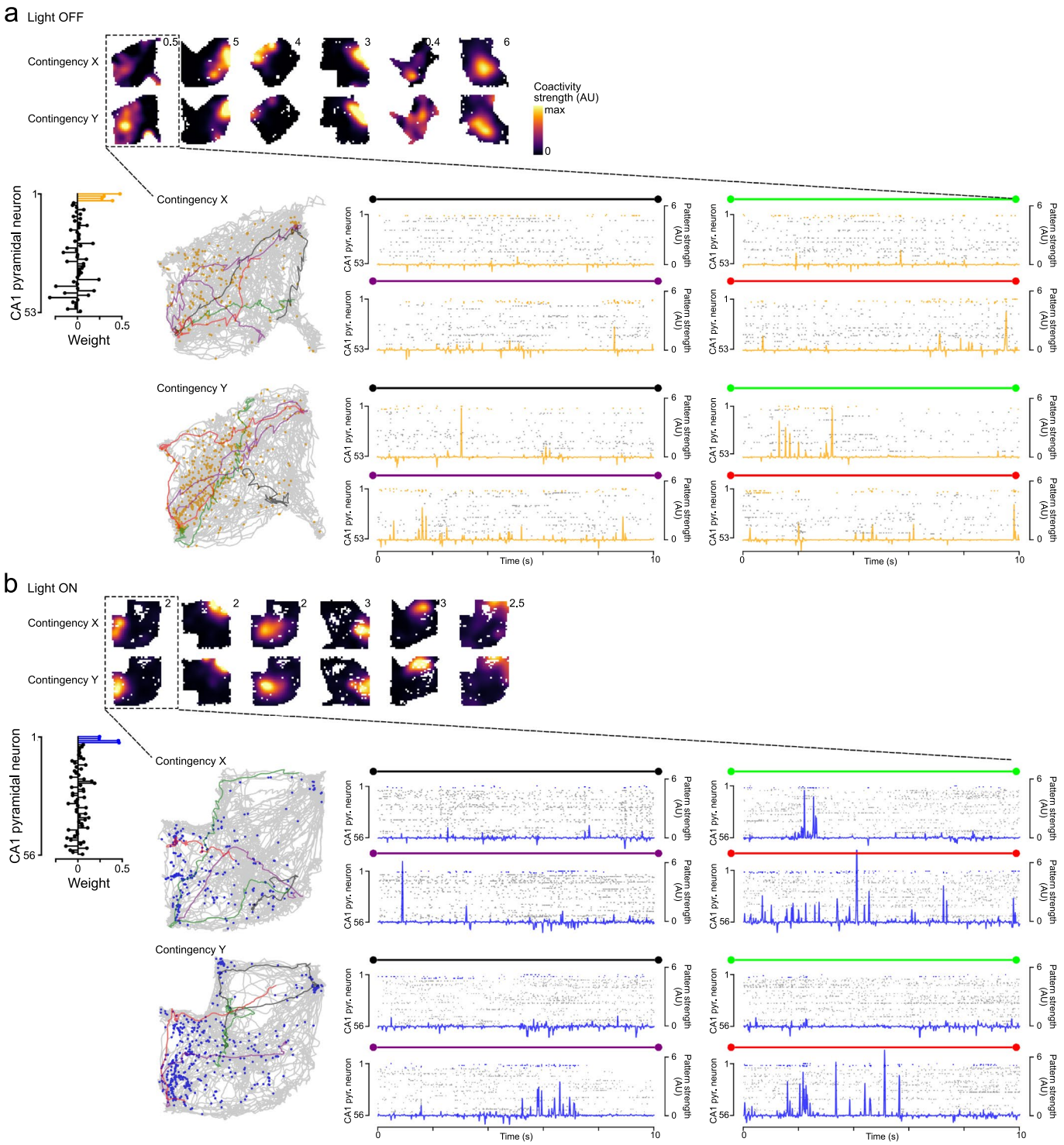

Extended Data Fig. 9 | Example coactivation maps and raster plots of principal neuron activity with or without left CA3-CA1 silencing. Example coactivity patterns during (**a**) light OFF and (**b**) $CA3^{L} \rightarrow$ CA1 input suppression (light ON) days across both learning contingencies (sessions X2 and Y2). Top of each panel depicts strength maps for several representative coactivity patterns, while below example coactivations for the left most pattern are shown in more detail. All coactivations (defined as coactivity strength above 2 standard deviation of mean strength in preferred contingency; displayed as coloured dots) are superimposed on coverage maps in each contingency (bottom left). Raster plots show the time-courses of neuronal firing (members color-coded orange or blue to denote contingency discriminating or contingency invariant pattern, respectively) and coactivation strengths for four separate paths (color-coded) across each contingency (bottom right) are plotted.

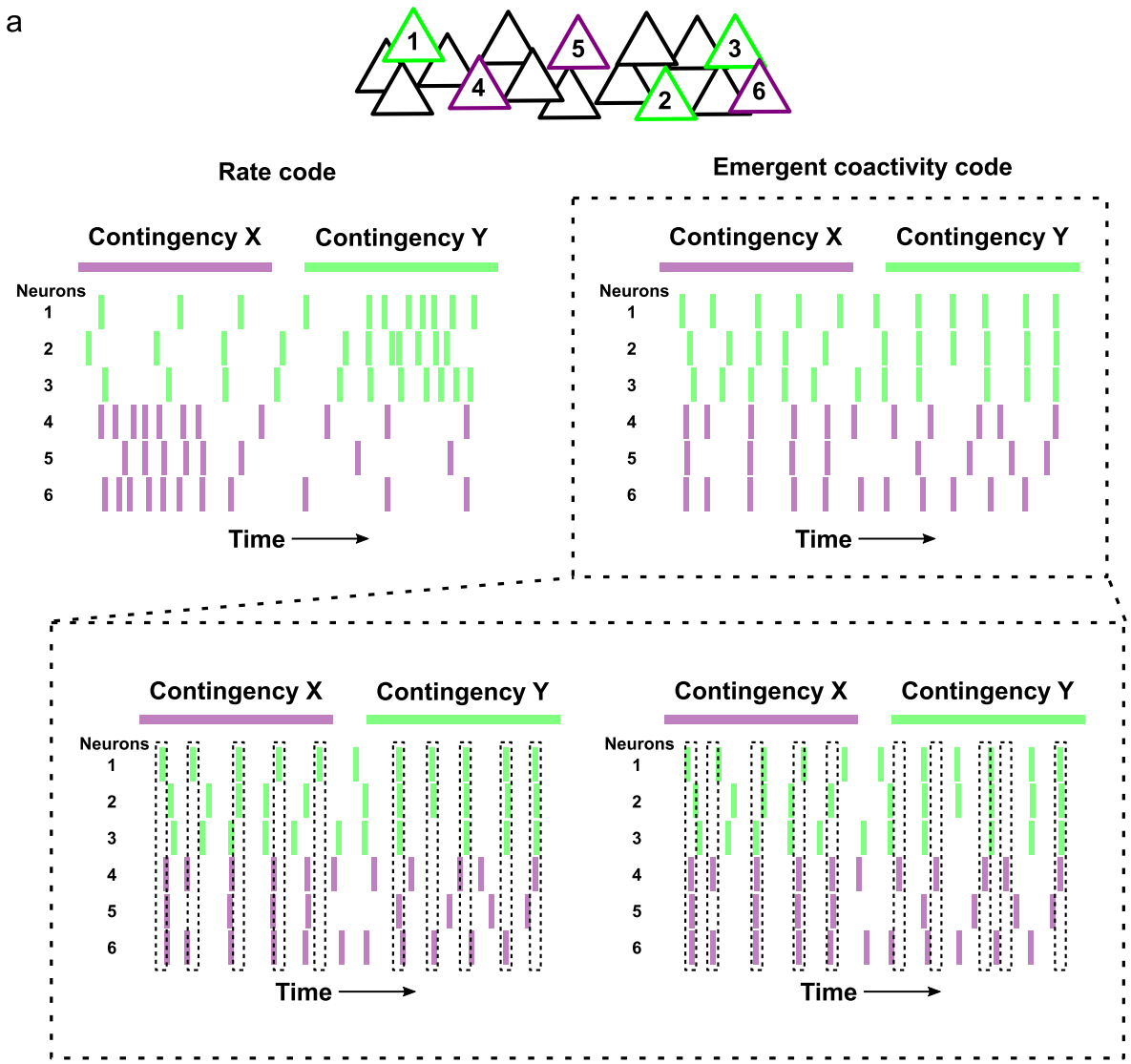

Extended Data Fig. 10 | See next page for caption.

Extended Data Fig. 10 | Schematic representation of emergent coactivity coding and a potential single-neuron reading mechanism. a, *Top*: Schematics contrasting a hypothetical rate code(Adrian, [1]) (left) and emergent coactivity code (right) for disambiguating contingencies. *Bottom*: Emergent coactivity code for contingencies with temporal windows indicated by dashed rectangles aligned to spikes from neuron 1 (left) or neuron 4 (right) showing that neurons 1, 2 and 3 are more coactive for contingency *Y* while neurons 4, 5 and 6 are more coactive for contingency *X*. **b**, A hypothetical 'reader' neuron can disambiguate distinct patterns of coactivity, for example by supralinear summation of one set of coactive inputs (for example from upstream neurons 1, 2 and 3), but only linear/sublinear summation of another (from upstream neurons 4, 5 and 6). Such non-linearities could result from the preferential activation of voltage-gated dendritic conductances, for example through clustering of synaptic inputs on dendritic branches (Stuart and Spruston, [48]). The membrane time-constant (~10-30 ms in forebrain pyramidal neurons (Koch et al., [9])) constrains a reader neuron's integration time-window, and hence this mechanism is particularly suited for short-timescale coactivity. Note that the converse may be true for another reader neuron, with inputs from neurons 4, 5, and 6 preferentially exhibiting supralinear summation and hence preferentially driving activity in this alternative neuron. Vm: membrane potential.

nature research

Corresponding author(s): Mohamady El-Gaby and David Dupret

Last updated by author(s): Jan 18, 2021

Reporting Summary

Nature Research wishes to improve the reproducibility of the work that we publish. This form provides structure for consistency and transparency in reporting. For further information on Nature Research policies, see our Editorial Policies and the Editorial Policy Checklist.

Statistics

For all statistical analyses, confirm that the following items are present in the figure legend, table legend, main text, or Methods section.

n/a	Confirmed
☐	☒ The exact sample size (*n*) for each experimental group/condition, given as a discrete number and unit of measurement
☐	☒ A statement on whether measurements were taken from distinct samples or whether the same sample was measured repeatedly
☐	☒ The statistical test(s) used AND whether they are one- or two-sided *Only common tests should be described solely by name; describe more complex techniques in the Methods section.*
☐	☒ A description of all covariates tested
☐	☒ A description of any assumptions or corrections, such as tests of normality and adjustment for multiple comparisons
☐	☒ A full description of the statistical parameters including central tendency (e.g. means) or other basic estimates (e.g. regression coefficient) AND variation (e.g. standard deviation) or associated estimates of uncertainty (e.g. confidence intervals)
☐	☒ For null hypothesis testing, the test statistic (e.g. *F*, *t*, *r*) with confidence intervals, effect sizes, degrees of freedom and *P* value noted *Give P values as exact values whenever suitable.*
☐	☒ For Bayesian analysis, information on the choice of priors and Markov chain Monte Carlo settings
☒	☐ For hierarchical and complex designs, identification of the appropriate level for tests and full reporting of outcomes
☐	☒ Estimates of effect sizes (e.g. Cohen's *d*, Pearson's *r*), indicating how they were calculated

Our web collection on statistics for biologists contains articles on many of the points above.

Software and code

Policy information about availability of computer code

Data collection	Neural data was acquired using the integrated circuit RHD2164 from Intan Technologies; and unit isolation was performed using KlustaKwik 2.0 and Kilosort 1.0 via the SpikeForest sorting framework. Confocal images were acquired using the ZEN (Zeiss Black 2.3) software.
Data analysis	Data were analyzed in Python 3.6 and and using the packages scikit-learn 0.23.2, statsmodels 0.12.1, Numpy 1.18.1, Scipy 1.4.1, Matplotlib 3.1.2, Pandas 0.25.3 and Seaborn 0.11.0.

For manuscripts utilizing custom algorithms or software that are central to the research but not yet described in published literature, software must be made available to editors and reviewers. We strongly encourage code deposition in a community repository (e.g. GitHub). See the Nature Research guidelines for submitting code & software for further information.

Data

Policy information about availability of data

All manuscripts must include a data availability statement. This statement should provide the following information, where applicable:

- Accession codes, unique identifiers, or web links for publicly available datasets
- A list of figures that have associated raw data
- A description of any restrictions on data availability

The data that support the findings of this study are available from the corresponding author upon reasonable request.

Field-specific reporting

Please select the one below that is the best fit for your research. If you are not sure, read the appropriate sections before making your selection.

☒ Life sciences ☐ Behavioural & social sciences ☐ Ecological, evolutionary & environmental sciences

For a reference copy of the document with all sections, see nature.com/documents/nr-reporting-summary-flat.pdf

Life sciences study design

All studies must disclose on these points even when the disclosure is negative.

Sample size	The dataset includes 1,124 neurons recorded from the dorsal CA1 of the Hippocampus. A total of 15 mice were used in this study. No statistical methods were used to pre-determine sample sizes but our sample sizes are similar to those reported in previous publications (e.g. ref 25,27,31,34,64).
Data exclusions	No mice were excluded. Inclusion criteria for well-isolated single units were used as published in previous studies and described in the methods section. Only recording days where mice covered a minimum of 50% of the open field were considered for analyses. Only probe sessions where animals covered at least 50% of the enclosure and completed at least 4 trials (i.e. visited at least one dispenser for at least 4 trials) were included in probe analyses.
Replication	The behavioural experiments were performed independently across mice (n=15) and recording days (n=71 light OFF training days; 43 light ON training days; 10 one-contingency learning light OFF days; 6 one-contingency learning light ON days). The electrophysiological analyses were performed independently across 853 neurons in light OFF days and 271 neurons in light ON days; 151 coactivity patterns in light OFF contingency X and 155 coactivity patterns in light OFF contingency Y, 56 coactivity patterns in light ON contingency X and 52 coactivity patterns in light ON contingency Y.
Randomization	Covariates were controlled using a within-subject, within-coactivity ensemble and within-cell design across conditions. Probe trials were presented in a random order of LED-defined contingencies.
Blinding	Data collection could not be performed blind to the conditions of the experiments since the experimenter had to be aware as to which conditions they had to expose each mouse on a given day (which behavioural task) and on a given session (which open field arena, Exploration versus Learning versus Probe, Light-delivery OFF versus ON). Neural and behavioural data analyses were conducted in an identical way regardless of the identity of the experimental condition from which the data were collected.

Reporting for specific materials, systems and methods

We require information from authors about some types of materials, experimental systems and methods used in many studies. Here, indicate whether each material, system or method listed is relevant to your study. If you are not sure if a list item applies to your research, read the appropriate section before selecting a response.

Materials & experimental systems

n/a	Involved in the study
☒	☐ Antibodies
☒	☐ Eukaryotic cell lines
☒	☐ Palaeontology and archaeology
☐	☒ Animals and other organisms
☒	☐ Human research participants
☒	☐ Clinical data
☒	☐ Dual use research of concern

Methods

n/a	Involved in the study
☒	☐ ChIP-seq
☒	☐ Flow cytometry
☒	☐ MRI-based neuroimaging

Animals and other organisms

Policy information about studies involving animals; ARRIVE guidelines recommended for reporting animal research

Laboratory animals	These experiments used adult male C57BL/6J mice (Charles River Laboratories, UK) or transgenic heterozygous Grik4-cre mice (The Jackson Laboratories; C57BL/6-Tg(Grik4-cre)G32-4Stl/J, stock number 006474, RRID: IMSR_JAX:006474; maintained on a C57BL/6J background). Mice were housed with their littermates until the surgical procedure with free access to food and water in a room with a 12/12h light/dark cycle, 19–23°C ambient temperature and 40–70% humidity. All mice held in IVC's, with wooden chew stick and nestlets. Mice were 4-7 months old at the time of testing.
Wild animals	No wild animals were used in the study.
Field-collected samples	No field collected samples were used in the study.

Ethics oversight	Experimental procedures performed on mice in accordance with the Animals (Scientific Procedures) Act, 1986 (United Kingdom), with final ethical review by the Animals in Science Regulation Unit of the UK Home Office.

Note that full information on the approval of the study protocol must also be provided in the manuscript.